MASTER'S THESIS

Dynamics of droplets on switchable prestructured substrates

Submitted by

MORITZ TEIGELKÖTTER

September 18, 2019

First examiner
PD Dr. Svetlana GUREVICH

Second examiner
Prof. Dr. Uwe THIELE

Westfälische Wilhelms-Universität Münster
Fachbereich Physik
Institut für theoretische Physik

CONTENTS

Appendix

NOMENCLATURE

Abbreviations

BC	Boundary Condition
FEM	Finite Element Method
HW	High wettability
LW	Low wettability
PDE	Partial Differential Equation

Symbols

Π	Disjoining or Derjaguin Pressure
R	Residual operator
ρ	Wettability contrast or wettability for homogeneous substrates
$C_0^\infty(D)$	Space of infinitely differentiable functions on the domain D
D	Physical domain
h	Film height
$L_2(D)$	Space of square Lebesque integrable Functions over the domain D
P	General pressure
Q	Mobility

1

INTRODUCTION

Nanostructured materials are prevalent in today's electronic industry. Many techniques have been established to produce nanostructures. Reference [1] gives an overview of processes involving wet coating techniques. In reference [2] the pattern formation mechanism in dip-coating experiments has been investigated with the help of long-wave approximations of the underlying hydrodynamic equations. Models based on the long wave approach have shown good agreements for a variety of experiments [3]. In particular, application of models based on long-wave expansions for spin coating can be found in [4, 5].

Prestructured substrates offer the possibility to control pattern formation. This has been employed experimentally (see e. g. [6, 7]) as well as theoretically (see e. g. [8, 9]) for vapor deposition on SiO_2 substrates with Au patterns. The theoretical investigations have shown that transversal instabilities destabilize the desired ridge solutions. The formation of Si and Ge nanocrystals via dewetting has been investigated using prestructured thin films as well [10].

In most experiments and theoretical investigations the wettability of the substrate was considered a static system property. However, it is possible to have light-induced changes in wettability, e.g. on polymer surfaces [11].

This thesis focuses on the theoretical investigation of the influence of switchable substrates, i. e. possibly prestructured substrates with dynamically changing wettabilities, on the dynamical behavior of a simple liquid or droplets consisting of a simple liquid. One aspect of the investigation is, whether switchable substrates can be an additional tool to influence the pattern formation mechanism. This is investigated on a theoretical basis with the help of a long-wave expansion model called thin-film equations (TFEs).

This system is mathematically modeled as partial differential equations (PDEs) which are capable of describing the temporal evolution of coupled or uncoupled spatially-extended variables. In this case the temporal evolution of the height profile of the fluid on a substrate is of interest. To relieve some conditions for the solution of the system the weak formulation is introduced. Together with the Galerkin Method the weak formulation forms the basis for the finite element method (FEM), which is employed for the numerical treatment of the system under consideration. The solutions of the system depends strongly on the choice of parameters. Continuation tools are employed to detect steady states and investigate their stability. Additionally direct numerical time solutions are used to increase the understanding of the temporal behavior of the solution in question.

This thesis is organized as follows: In chapter 2 the theoretical model is presented. Computational details can be found in chapter 3. The functional principle of the developed interface to communicate data between the employed software is explained in chapter 4. In chapter 5 a homogeneous switchable substrate is investigated, before a prestructured substrate is investigated in chapter 6. Finally, chapter 7 summarizes the results and gives an outlook on possible future investigation.

2

THEORETICAL MODEL

2.1 GOVERNING EQUATIONS

The system of interest is a flat liquid film on a prestructured substrate with a switchable wettability. Such a system can be modeled based on the thin-film equation (cf. [8, 9, 12]). The general form of the non-dimensionalised thin-film equation is

$$\partial_t h(x,t) = \nabla \cdot \{Q(h)\nabla[P(h,x,t)]\}. \tag{2.1}$$

For details on the non-dimensionalisation cf. [8]. The film height is h, $Q(h) = h^3$ is the mobility resulting from no-slip boundary conditions at the substrate[1] and $P(h,x,t)$ is a general pressure. The evolution of the film height h corresponds to a conservation law and can be alternatively formulated in gradient dynamics form [9, 13] as

$$\partial_t h = -\nabla \cdot j = \nabla \left[Q(h)\nabla \frac{\delta F_0}{\delta h} \right] \tag{2.2}$$

with the flow j and the free energy potential F_0, which is discussed more in detail in section 2.2. The origin of the thin-film equation is the Navier-Stokes equation. The key idea in the derivation of the thin-film approximation from the Navier-Stokes equation is that the lateral length scale is higher than the length scale of the film height. Such an approximation can also be called long-wave approximation. A detailed derivation from the Navier-Stokes equation can be found in reference [14]. The thin-film equation can be applied to study a variety of phenomens. It has been used to investigate spin-coating [4, 5] and dip-coating [2]. Droplets on an inclined plane can also be described with the thin-film equation [15].

The free energy F_0 has to be adapted depending on what shall be described with the thin-film equation. In this work the variation of the free energy with respect to the film height $\frac{\delta F_0}{\delta h}$, which is the general pressure P, consists of two parts

$$P(h,x,t) = -\Delta h - \Pi(h,x,t), \tag{2.3}$$

where $\Pi(h,x,t)$ is the so-called Derjaguin or disjoining pressure and the term $-\Delta h$ is called Laplace pressure. The disjoining pressure is chosen to be

$$\Pi(h,x,t) = \left(\frac{1}{h^6} - \frac{1}{h^3}\right)(1 + \rho g(x,t)). \tag{2.4}$$

---

[1] Strong slip boundary conditions yield a mobility $Q \propto h^2$ and a mobility $Q \propto h$ can be used to investigate transport via diffusion [8].

The first term $\left(h^{-6} - h^{-3}\right)$ can be derived and modeled by a variety of different ansätze. For a detailed explanation and further literature cf. [14]. The term $(1 + \rho g(x,t))$ allows for a prestructured and switchable substrate similar to [8, 9, 14]. The product $\rho g(x,t)$ is called wettability with the wettability contrast ρ. For a homogeneous substrate, i. e. $g(x,t) = 1$, the term wettability can refer only to the parameter ρ. The wettability modulates the macroscopic equilibrium contact angle Θ_0 according to

$$\Theta_0 = \sqrt{\frac{3}{5}(1 + \rho g(x,t))}. \tag{2.5}$$

Notice that the film height is scaled different from the lateral lengths to get the non-dimensionalised form of equation (2.1) and consequently the contact angles are scaled as well. To help visualize the results contact angles are still given in degrees.

In this mesoscopic model a minimum film height called precursor film height h_p is necessary to model the transition between a wetted and a dewetted substrate [14]. Consequently, there is no sharp line of contact in the mesoscopic image. Instead there is a contact region. In the case of the non-dimensionalised TFE the precursor film height is $h_p = 1$. For stationary states, i. e. $\partial_t h = 0$, integrating twice leads to

$$\triangle h + \Pi(h,x,t) + C = 0, \tag{2.6}$$

where C is an integration constant corresponding to a constant pressure inside the film characterizing mechanical equilibrium. As "mass" is conserved in the system the first integration constant corresponding to the net flux is zero [8]. This form can be used for continuation purposes as done in [8]. For linear stability analysis the full form (2.1) has to be considered. In this work the full form is always employed. For further computational details cf. chapter 3.

2.2 FREE ENERGY

The general pressure term $P(h,x)$ can be expressed as a variation of a free energy potential [9, 13]

$$P(h,x,t) = \frac{\delta F_0[h]}{\delta h}. \tag{2.7}$$

Here the the free energy is defined as

$$F_0[h] := \int_D \left[\frac{1}{2}(\nabla h)^2 + V(h)\right] \mathrm{d}\vec{x} \tag{2.8}$$

$$\text{with} \quad V(h) = \left[-\frac{1}{2h^2} + \frac{1}{5h^5}\right](1 + \rho g(x,t)). \tag{2.9}$$

The first term under the integral in equation (2.8) corresponds to a surface energy in the thin-film approximation and results in the Laplace pressure term $-\Delta h$. The second term relates to the disjoining pressure, as it can be derived with $\Pi(h, x, t) = \partial_h V(h)$. Furthermore, the film height $h(x, t)$ and the mobility $Q(h) = h^3$ are positive semidefinite and the mean film height is conserved, so that $F[h]$ is a Ljapunov functional for the system [14]. This implies that $h(x, t)$ changes in time, in such a way that $F[h]$ is minimized. This plays an important role, as it offers a direct way of checking whether direct numerical simulations yield a plausible result. Additionally, it can be used as a measure for bifurcation diagrams, which provides additional information about the global stability. The absolute value of the free energy can be shifted arbitrarily. In all the calculations presented here, the free energy $F_{0,rel}$ is calculated relative to a homogeneous film and normalized to the volume

$$F_{0,rel} := \frac{1}{D}\left(F_0[h(x)] - F_0[h_0]\right). \tag{2.10}$$

Here h_0 is the mean film height and consequently the film height of the homogeneous film. A value of $F_{0,rel} = 0$ corresponds to the free energy of a homogeneous film, which makes it easier to state whether any other steady state has a higher or lower free energy and thus if such a state can collapse to the homogeneous film or not. In the following the relative free energy will be denoted with F_0 as no other free energy is used.

3

COMPUTATIONAL DETAILS

For the numerical treatment two packages are employed. The Matlab[16] package PDE2PATH [17, 18] is used for continuation and linear stability calculations. The C++ library OOMPH-LIB [19] is used for direct numerical simulations. Both packages rely on the Finite Element method.

3.1 FINITE ELEMENT METHOD

The Finite Element Method (FEM) is a numerical approximation method which can be used to solve PDEs. The weak formulation combined with Galerkins method builds the mathematical backbone for the finite element method.

3.1.1 *Weak Formulation*

The mathematical model for a physical, spatially-extended system usually consists of one or more PDEs, a finite spatial domain and appropriate boundary conditions (BCs). Sometimes additional constraints have to be considered as well. Consequently, statements about existence and uniqueness of classical solutions cannot be made easily. A classical solution is a solution, which is differentiable at every point in the domain as often as required by the PDE. Therefore the so-called weak solution is introduced, which does not require the desired solution to be differentiable in the classical sense, i. e. the weak solution is not necessarily a classical solution [20]. Nevertheless, a weak solution can be a classical solution. Ultimately, the weak solution enlarges the solution space by relieving differentiability criteria for the solutions.

Consider a one-dimensional nonlinear PDE for a function $u(x,t)$

$$f(u,x,t) + \frac{\partial u(x,t)}{\partial x} + \frac{\partial^2 u(x,t)}{\partial x^2} - \frac{\partial u(x,t)}{\partial t} = 0 \tag{3.1}$$

on the domain D fulfilling certain boundary conditions. These boundary conditions can be Dirichlet BCs, i. e. the value of the solution at the boundary of D is fixed, Neumann BCs, i. e. the normal derivative at the boundary is fixed, any kind of suitable mixed BC or Robin BCs, i. e. a weighted combination of Dirichlet and Neumann BCs, as well as periodic BCs. The residual operator R is defined in such a way that $\mathrm{R}\left[u\right] = 0$ is equivalent to 3.1.

Before PDEs can be formulated weakly, the weak derivative has to be defined. Consider the function space $L_2(D)$ containing all functions

u, which are square integrable over D. Two functions u and v can be identified with eachother, if $u(x) = v(x)$ for $x \in D$ except for a null set O (i. e. $\int_O \mathrm{d}x = 0$). The scalar product $(u, v)_{L_2}$ is defined [20] as

$$\langle u, v \rangle_{L_2} := \int_D u(x)v(x)\mathrm{d}x. \tag{3.2}$$

The weak derivative of u denoted $v = \partial^\alpha u$ can be defined [20], if $v \in L_2(D)$ and

$$\langle \phi, v \rangle_{L_2} = (-1)^{|\alpha|} \langle \partial^\alpha \phi, u \rangle_{L_2} \qquad \forall \phi \in C_0^\infty(D). \tag{3.3}$$

Here $C_0^\infty(D)$ is the space of infinitely differentiable functions on D. If a function is differentiable in the classical sense, it is also weakly differentiable and both derivatives are the same [20].
The weighted residual r for the weak solution u_w is defined as

$$r = \int_D \mathrm{R}\,[u_w]\phi^{\mathrm{test}}\mathrm{d}x, \tag{3.4}$$

where R is the residual operator correspond to equation 3.1. If a function u_w satisfying the boundary conditions is found and suitable test functions ϕ^{test} are chosen, the residual vanishes. To understand what makes a test function suitable the following expression is considered and integrated by parts

$$\int_D \frac{\partial^2 u_w}{\partial x^2}\phi^{\mathrm{test}}\mathrm{d}x = \left.\frac{\partial u_w}{\partial x}\phi^{\mathrm{test}}\right|_{\partial D} - \int_D \frac{\partial u_w}{\partial x}\frac{\partial \phi^{\mathrm{test}}}{\partial x}\mathrm{d}x. \tag{3.5}$$

For Neumann boundary conditions the boundary term in equation (3.5) vanishes without further constraints for the test function space as $\partial_x u_w = 0$ on ∂D. This is the reason Neumann boundary conditions are sometimes called natural boundary conditions [20]. In contrast, the boundary term does not vanish for Dirichlet boundary conditions. Only with the help of the constraint $\phi^{\mathrm{test}} = 0$ on ∂D for the test function space the boundary term vanishes.

3.1.2 *Galerkin Method*

The Galerkin Method provides a method to approximate the solution of the variational problem (3.4). Suppose $u_w(x)$ satisfies Neumann, it can be expanded into an infinite set of basis functions $\psi_j(x)$

$$u(x) = \sum_{j=1}^{\infty} U_j \psi_j(x) \tag{3.6}$$

with the expansion coefficients U_j. Inserted back into (3.4) gives

$$r = \int_D \mathrm{R}\left(x, \sum_{j=1}^{\infty} U_j \psi_j(x)\right)\phi^{\mathrm{test}}(x)\mathrm{d}x = 0. \tag{3.7}$$

Notice that this equation has to hold for any $\phi^{\text{test}} \in C_0^\infty$ and that $\{\psi_j\}$ has to form a complete basis for the underlying function space. Thus ϕ^{test} can also be expanded into the same basis yielding

$$r = \sum_{k=1}^{\infty} \Phi_k r_k(U_1, U_2, \dots) = 0 \tag{3.8}$$

with the expansion coefficients Φ_k and

$$r_k = \left\langle \mathrm{R}\left(x, \sum_{j=1}^{\infty} U_j \psi_j\right), \psi_k \right\rangle_{L_2} \tag{3.9}$$

Equation (3.8) has to hold for any values for Φ_k, which is equivalent to $r_k = 0$ for all possible values of k.

So far the treatment has been exact. To approximate the solution u_w and decrease computation time, the expansion of $u_w(x)$ and the test function ϕ^{test} can be truncated and a finite number M of basis functions can be used. As $M \to \infty$ the approximation approaches the exact value of u_w. The result is a system of algebraic equations for the unknown coefficients U_j, $j = 1, \dots, M$

$$r_k(U_1, U_2, \dots) = 0 \quad \text{for} \quad k = 1, \dots, M, \tag{3.10}$$

which can be solved with several different of algorithms like the iterative Newton method.

The Galerkin method is also applicable for other boundary conditions. The solution u_w only has to be split up in two parts, where one part satisfies the essential boundary conditions and the other part satisfies the natural boundary conditions. In the case of Dirichlet boundary conditions it has the form

$$u_w = u_p + u_h \quad \text{where} \quad u_h|_{\partial D} = 0 \text{ and } u_p|_{\partial D} = g, \tag{3.11}$$

where g is the value u_w is supposed to be on ∂D. The only difference to the case described above is the term u_p, which has to be carried through the whole calculation.

3.1.3 *Functional Principle*

The initial step in the Finite Element Method is to divide the domain D into elements d_i such that $D = \cup_i d_i$. An element consists of nodes that lie on its circumference. For the nodes basis functions with a finite support, which are only nonzero on a few (often only on the next-neighboring) nodes and build a basis for the function space of $u_w(x)$, have to be chosen. Adjacent elements share common nodes connecting all the elements. The weak formulation plugged into the Galerkin method yields a sparse residual matrix, which can then be solved with a Newton solver.

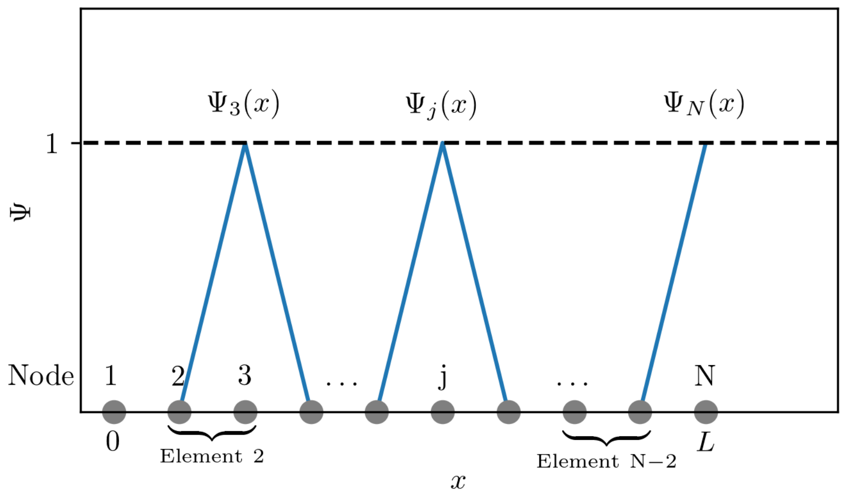

Figure 3.1: An example of shape functions in 1D. The shown linear shape functions $\Psi_i(x)$ are sometimes also called "hat"-functions. The function $\Psi_i(x)$ corresponds to the i-th node. Nodes are shown as grey markers and are numbered above. Two elements grouping the nodes are shown exemplary.

A example of widely used basis functions is shown in Figure 3.1 on a domain D with length L. In this example every element has two nodes, which connect itself to the adjacent elements. Figure 3.2 shows a problem which can occur if elements of different sizes are involved in 2D. On the left panel the red node belongs to the right element but not to the left. The red node is called a hanging node[20]. To resolve this issue the bigger element on the left is split into two smaller elements. This problem is usually solved by the employed FEM library itself.

POSSIBLE ENHANCEMENTS OF THE FEM The FEM approximation converges to the exact solution in the case of infinitely many elements. Thus in general a finer mesh yields more accurate results on the cost of a higher computational time. Usually the required accuracy and resolution of the mesh varies across the domain, e. g. a localized solution does not need a high spatial resolution in regions where it is close to constant. The FEM allows to resolve different regions of the domain with different levels of accuracy. Another method to achieve higher accuracy is the use of higher order basis function like polynomials of third order. So far the theory has only dealt with solutions for one specific time. For time stepping the whole array of known time steppers also applicable for finite difference methods can be applied. For time simulations it is possible to change the number and size of the elements at each time step. This is called adaptive mesh size.

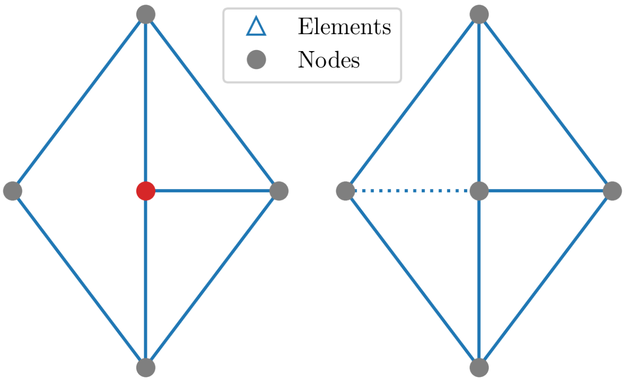

Figure 3.2: Left: Example of a hanging node in a 2D triangular mesh. The hanging node is marked red. The other nodes are marked grey. Right: Introduction of a new element with the dotted line to avoid the hanging node.

3.2 CONTACT ANGLE CALCULATION

A droplet can be characterized with the help of the contact angle. Measuring a contact angle within a thin-film model is not trivial due to the precursor film. A first approach can be to calculate the contact angle Θ from the steepest slope of the droplet according to

$$\tan \Theta_{\text{slope}} = \max \frac{\partial h}{\partial x} \quad \text{with} \quad x \in D. \tag{3.12}$$

This is easy to calculate in an automated way, if there is only one droplet in the domain. This angle can be referred to as the mesoscopic contact angle. For a comparison with experimental results and other theoretical models the macroscopic contact angle is necessary.
The macroscopic contact angle can be measured with a circular fit of the droplet with the fitting function

$$h_{\text{fit}}(x) = \sqrt{R^2 + (x - x_c)^2} + y_c, \tag{3.13}$$

where (x_c, y_c) is the center of the circle and R its radius. Figure 3.3 shows an example of a droplet fitted to a circle. The initial guess, which is calculated from the point of maximum height and the two points with the steepest slope is shown as well.
To diminish the influence of the precursor film the data ranged used for fitting needs to be limited. For this only data points above a certain fraction of the maximum height are considered, i. e. data points which satisfy

$$h(x) > c \cdot h_{\text{max}}. \tag{3.14}$$

This procedure is suitable for all droplet heights. The choice $c = 2/3$ and its dependency on the contact angle measurement are discussed in

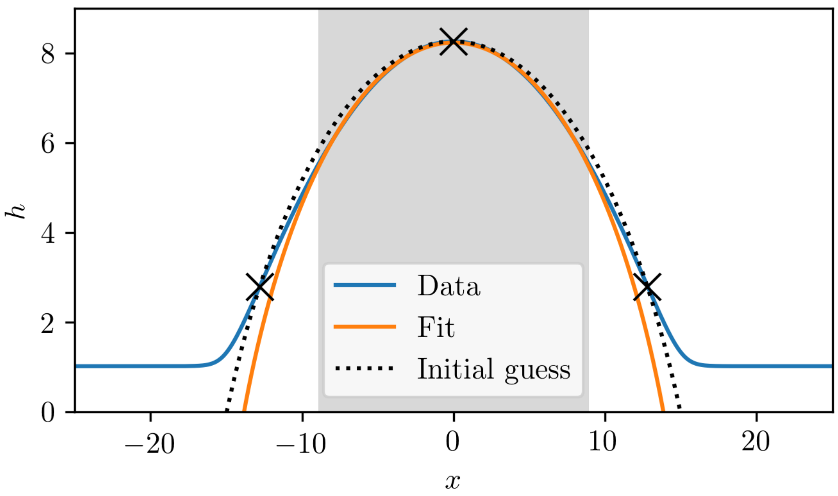

Figure 3.3: Examplary circular fit to a droplet to determine the contact angle. The marked points are used to calculate the initial guess of the fit. The shaded region marks the data range which is used to fit the function (3.3).

section 5.1. The fit itself is computed with a least-squared Marquardt-Levenberg algorithm [21, 22]. The contact angle Θ_{fit} can then be calculated similar to (3.12) via the slope at the precursor film height h_p

$$\tan \Theta_{\text{fit}} = \left.\frac{\partial h_{\text{fit}}}{\partial x}\right|_{h=h_p}. \tag{3.15}$$

In the following Θ without the subscript will refer to the macroscopic equilibrium contact angle determined through the circular fit. As a default value for a higher wettability $\rho_{\text{HW}} = -0.12$ is chosen. For less wettable areas $\rho_{\text{LW}} = 1.96$ is chosen. These wettabilities correspond to contact angles of 40° and 75° respectively. A detailed discussion of measured contact angles and the relation to the theoretical expectation from equation (2.5) can be found in section 5.1.

3.3 PDE2PATH

The Matlab package PDE2PATH can deal with second order PDEs. The thin-film equation (2.1) is of forth order. Therefore it is implemented as a two dimensional system of second order PDEs, which are given in residual formulation as

$$0 = \nabla \cdot \left\{h^3 \nabla \beta\right\} - \partial_t h \tag{3.16}$$

$$0 = -\triangle h - \Pi(h, x, t) - \beta. \tag{3.17}$$

Equation (3.17) defines the auxiliary variable β, which corresponds to the general pressure in equation (2.3). As the system is invariant under a change of "mass", i. e. a change in mean height h_0, there is always a neutral eigenvalue corresponding to the present Goldstone mode. If h_0 is not a free continuation parameter, the drifting along the Goldstone mode is suppressed with the constraint q_1

$$q_1 := h_0 - \frac{1}{D} \int_D h \mathrm{d}x = 0. \tag{3.18}$$

Periodic boundary conditions imply that for any Δx the height profile $h(x + \Delta x)$ is a solution of the system, if $h(x)$ is a solution. For solutions with a translational symmetry this does not pose a problem as the corresponding orbit of solutions is a single point in solution space. For any solution without translational symmetry the constraint q_2

$$q_2 := \int \frac{\partial h_{\mathrm{old}}}{\partial x} (h_{\mathrm{new}} - h_{\mathrm{old}}) \mathrm{d}x = 0 \tag{3.19}$$

has to be introduced. Here h_{old} is the height profile of the previous time step and h_{new} is the next height profile to be calculated. This avoids following the orbit of solutions, which are equivalent under translation.

As measures to display bifurcation diagrams the relative free energy introduced in (2.10) and the maximum height $h_{\max} = \max h(x)$ are used additional to the L^2 norm $\|h\|_2$.

3.4 OOMPH-LIB

Continuation is useful to get a first insight about the dynamics of a system. For a more detailed analysis of the dynamics direct numerical time simulations are unavoidable. Finite difference method lack a numerical stability for all combinations of the time step Δt and the spatial resolution Δx. The Object-Oriented Multi-Physics Finite Element Library (OOMPH-LIB) [19] provides an open-source implementation of the FEM and a method for time integration with an adaptive step size among others implemented in C++.

The adaptive time stepper proves especially useful as different timescales are involved in the dynamics to decrease computational time. Additionally, it can be used as a heuristic to detect steady states. If the time steps passes a certain threshold Δt_{tr}, the current state $h(x)$ can be regarded as a steady state. If not stated otherwise the value $\Delta t_{\mathrm{tr}} = 1 \times 10^6$ is used.

The relaxation of a height profile $h(x)$ does not necessarily develop directly to the final state. The free energy F_0 can stay close to constant for a certain time before converging to the final state. Such a state is called meta state. If meta states are involved, the total relaxation times can get long compared to the relaxation time with no meta state involved. In such cases the meta state plays an important role for real life problems. Without a meta state the assumption that the free energy decreases exponentially could give relaxation times via a fit. Though, there is no reason why the free energy should decrease exponentially. The relaxation time $\tau[f]$ for any function $f(t)$ is defined as

$$\tau[f(t)] := \int_0^\infty \frac{f(t) - f_\infty}{f_0 - f_\infty} \mathrm{d}t \tag{3.20}$$

with the initial value $f_0 = f(t = 0)$ and the value it converges to $f_\infty = f(t = \infty)$.

An advantage of this definition is that it can always be calculated even when a fitting process would fail. Additionally, it makes it possible to discuss relaxation times independent of the accurate, actual shape of $f(t)$. The function $f(t)$ can refer to any time-dependent variable, which converges monotonically towards a steady value. This can be the free energy $F_0(t)$ as well as the contact angle $\Theta(t)$ or any other measure. Notice that the function $\Theta(t)$ is not a Ljapunov functional and can behave non-monotonically. With this the definition a function, which stays at some intermediate value for some time and then decreases fast, cannot be distinguished from a slowly but steadily decreasing function. This issue can be solved with the introduction of the first moment

$$\tau_1[f(t)] := \int_0^\infty t \cdot \frac{f(t) - f_\infty}{f_0 - f_\infty} \mathrm{d}t. \tag{3.21}$$

A steadily decreasing function has a lower first moment than a function with step-like behavior. Comparing the relaxation times and the its first moments for two different situations allows to make statements about the evolution of the free energy. Nevertheless, the complete evolution of $f(t)$ has to be considered to get a full grasp of the situation. Numerically it is not possible to integrate until $t = \infty$. Instead, time is integrated till t_{tr}, as $f(t_{\mathrm{tr}}) \approx f(t = \infty)$.

Any continuation step in general consists of a predictor and a corrector step [23]. The predictor calculates a guess for a slightly changed set of parameters and the corrector tries to converge the predictor's guess towards a solution of the underlying system. A simple predictor takes the tuple $\left(h^i(x), \lambda^i\right)$ and changes the continuation parameter λ by a small value $\mathrm{d}\lambda$

$$\left(h^i(x), \lambda^i\right) \to \left(h^{i+1}(x), \lambda^{i+1}\right) = \left(h^i(x), \lambda^i + \mathrm{d}\lambda\right). \tag{3.22}$$

To converge the predictor's guess to a stationary solution a direct numerical time simulation can be employed as the corrector. This scheme has been implemented in OOMPH-LIB and helps to get an overview of the stable states. Notice that a hysteresis is likely to occur at bifurcation points for small $\mathrm{d}\lambda$, where the stability changes.

4

DATA TRANSFER BETWEEN PDE2PATH AND OOMPH-LIB

A smooth work-flow with two different packages requires an interface to propagate data from one package to the other. pde2path uses the proprietary default Matlab file format `.mat`, which can be easily loaded into Matlab but not into other packages written in other languages. As a workaround the commands `dlmwrite` or `writematrix`[1] can be used to write standard `.dat` files which can then be loaded from other programs. Matlab offers a Matlab Engine API and a Matlab Data API for C++. The Matlab Engine API's purpose is the interaction with an instance of Matlab, whereas the Matlab Data API provides C++ data types to store Matlab data in a C++ program. These APIs only need a valid Matlab license to work.

The developed interface consists of two parts. The first parts loads the files into the Matlab Engine and then casts the necessary information into oomph-lib and C++ data types such as `oomph:Vector<double>` and `int`. The second part takes the data read from the `.mat` file and interpolates the values for the nodes used in the oomph-lib mesh. This necessary as the data transfer has to work independently from the specific meshes and mesh resolutions used. The following sample code starts an instance of Matlab, loads a pde2path problem struct and extracts the variable named `nu`, which is a field in the `1x1 struct p`. The Matlab variable `nu` is first saved as a variable of type `Reference<TypedArray<double>>`. This data structure can generally hold an array of arbitrary size. In this case it is known that `nu` is only one number and can thus be saved as an `int`.

```
//Start MATLAB engine synchronously
std::unique_ptr<MATLABEngine> matlabPtr = startMATLAB();
//Evaluate expression in MATLAB
matlabPtr->eval(u"p=loadp('testfile.mat')")
//Import variable from MATLAB
StructArray p = matlabPtr->getVariable( u"p");
//Extract desired variable from struct
Reference<TypedArray<double>> nuval = p[0]["nu"];
int nu = *nuval.begin();
//Terminate MATLAB engine
terminateEngineClient();
```

---

[1] Starting from version R2019a the command `writematrix` should be used (cf. `https://de.mathworks.com/help/matlab/ref/dlmwrite.html`, last accessed 06.08.2019)

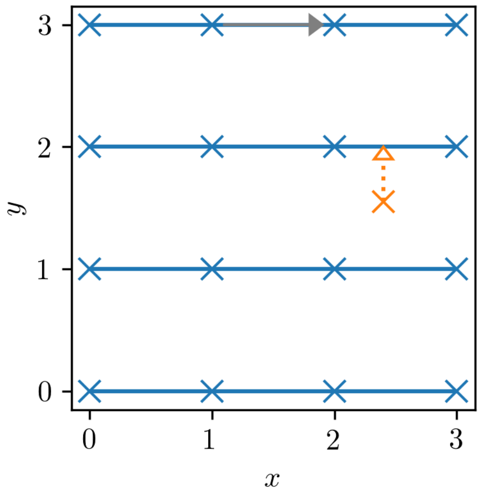

Figure 4.1: Visualisation of the way points are stored and the 2D interpolation used in the interface. The orange cross marks a point, for which the interpolation is calculated. The blue crosses represent data points read from the Matlab data file. The gray arrow indicates how the two dimensional points are saved row by row in a one dimensional array.

Similarly all the relevant values like the number of equation `p.nc.neq` and the number of discretization points `p.np` can be extracted. Using the workaround via `.dat` files requires a sophisticated file format or multiple files to make all the variables available to other programs. Usually in practice necessary variables are hard coded, which means that the interface code would have to be strongly adapted each time it is used for another problem or even with other settings. The Matlab Engine API and Matlab Data API make it possible to formulate such an interface more generally. Another advantage is that the otherwise created `.dat` files are not necessary anymore and disc space is saved. The second part of the interface deals with the problem that the nodes in PDE2PATH and OOMPH-LIB are not necessarily at the same position. Consequently interpolation needs to be implemented. A sophisticated interpolation is not necessary, because the Newton solver applied by OOMPH-LIB can deal with minor deviations. For 1D problems a linear interpolation is implemented. Figure 4.1 helps to visualize how the interpolation in 2D is implemented. The grey arrow indicates the order, in which points are stored row by row in a one dimensional array. As no high accuracy is required and the algorithm shall be as fast as possible, the position is projected onto the next line of data points and then a linear interpolation is performed. This avoids jumping within the one dimensional array of data points.

5

DROPLET ON A HOMOGENEOUS SUBSTRATE

Before an inhomogeneous prestructured surface is considered, the dynamics of a droplet on a homogeneous substrate, i. e. $g(x) = 1$, is investigated. The temporal transition between different wettabilities can occur very differently, so at first an instantaneous switch between two wettabilities is considered. An instantaneous switch of the wettability means that at a time T the wettability ρ is changed from the previous value ρ_1 to another value ρ_2 and the prestructure does not change. Before such a system can be investigated, some preparatory work has to be done first.

5.1 EQUILIBRIUM CONTACT ANGLE

To have better means of discussing what happens to the droplets on the surface, the droplets need to be characterized. As a measure, which is accessible in experiments and every other theoretical model, the contact angle stands out. In chapter 3 it is described, how it can be determined from a given height profile $h(x)$. Finite Size Effects can alter the contact angle as well as the data range used for fitting.

Figure 5.1 shows the computed contact angle Θ for different values of ρ compared with literature values according to equation (2.5). The qualitative shape is comparable for all the methods. The contact angle measurement on a bigger domain with $L = 200$ and the same net droplet volume validates that finite size effects do not play a role for droplets with a maximum width of 25 on a domain with $L = 100$. The maximum difference for $\rho < 3$ between the measurements with different domain size is smaller than $1°$, which is negligibly small. For $\rho < 2$ it is even in the range of $0.1°$. Bigger deviations only occur for values of ρ where the contact angle approaches $90°$. The contact angle determined via the fit Θ_{fit} fluctuates systematically between $0.86°$ and $1.65°$ below Θ_{lit}. Compared to the contact angle determined via the steepest slope Θ_{slope} the literature value Θ_{lit} is much higher. In Figure 5.1 the difference between Θ_{slope} and Θ_{lit} rises up to $38°$. This emphasizes that Θ_{slope} should not be used to characterize droplets and compare results with other models.

The influence of the data range used for fitting is shown in Figure 5.2. The criterion $h > 2/3 \cdot h_{\text{max}}$ has shown to provide reliable results. Figure 5.2 shows the measured contact angle for the data points with $h > \frac{1}{2}h_{\text{max}}$. For this criterion the difference to Θ_{lit} grows monotonically from $1.8°$ to $6°$.

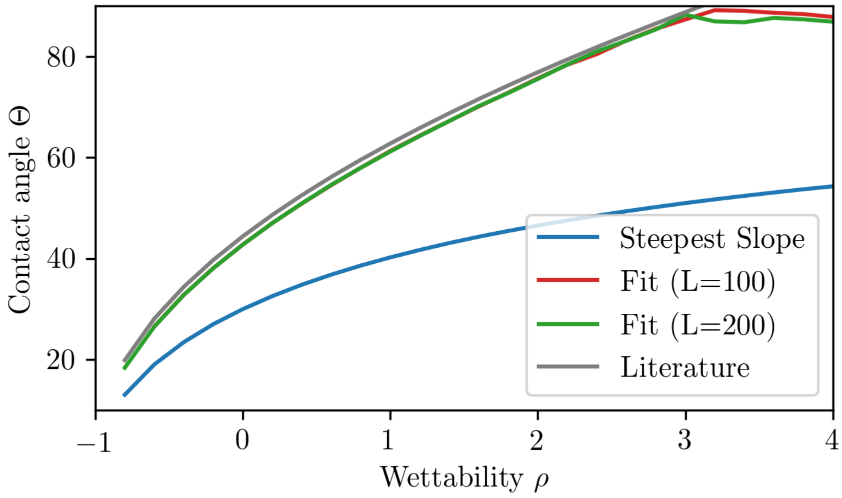

Figure 5.1: Dependency of the equilibrium contact angle Θ on the wettability ρ for a domain size $L = 100$ with mean height $h_0 = 3$ and for a domain size $L = 200$ with a mean height $h_0 = 2$. The mean heights are chosen in such a way that the net droplet volume stays the same. The contact angle measured with a circular fit is compared to the contact angle calculated from the steepest slope and the literature values according to (2.5).

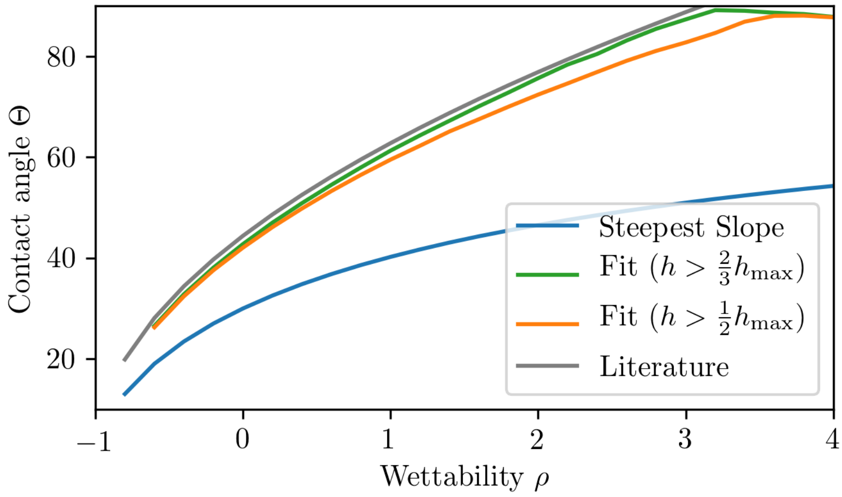

Figure 5.2: Dependency of the equilibrium contact angle Θ on the wettability ρ for a domain size $L = 100$ with mean height $h_0 = 3$ for different cutoffs used for fitting. As a reference the contact angle calculated from the steepest slope and the literature values according to (2.5) are given.

5.2 CONTINUATION FOR CONSTANT WETTABILITY

The choice of ρ influences the available steady states, as well as the range, where those steady states occur. A thorough understanding of the system with a time-independent wettability is a necessary foundation for the investigation of a switchable wettability.

The continuations shown in Figure 5.3 show continuation runs in the parameter h_0 for the parameters $\rho_{\mathrm{HW}} = -0.12$ and $\rho_{\mathrm{LW}} = 1.96$. These are the default values used throughout this thesis for the highly wettable (HW) and the low wettable (LW) scenario. The lower value for ρ is called highly wettable, because a lower value for ρ implies that the system is more likely to be wetted.

Starting from a homogeneous steady state the first bifurcation point is expected at $h_0 = \sqrt[3]{2} \approx 1.26$ for both wettabilities according to analytical results from [14]. The continuations in Figure 5.3 are consistent with this analytical result. At this bifurcation point the droplet steady state emerges subcritically. Other branches with multi droplet steady states emerge simultaneously at this bifurcation point. In Figure 5.3b a branch with four droplets for ρ_{LW} is shown.

At the bifurcation point with $h_0 = \sqrt[3]{2}$ the homogeneous steady state becomes linearly unstable. The homogeneous steady state for $L = 100$ becomes stable again at the bifurcation with $h_0 = 5.07$ and $h_0 = 6.88$ for the higher and the lower wettability respectively. For a smaller domain ($L = 50$) these values are $h_0 = 3.51$ and $h_0 = 4.85$ respectively. This indicates a domain dependency in the sense that the section, where the homogeneous steady state is linearly unstable, can be extended by increasing the domain size. Another important point in the continuation plots is the point, where the droplet steady state has a relative free energy of $F_0 = 0$ and thus crosses the free energy of the homogeneous branch. For $L = 100$ this transition occurs at $h_0 = 8.21$ and $h_0 = 14.00$ for the higher and the lower wettability respectively. For $L = 50$ these values are $h_0 = 4.63$ and $h_0 = 7.62$ respectively. For a planar geometry there is no direct physical meaning behind these points. They result from the numerical restriction to a finite domain and the employed periodic boundary conditions. However, they can serve as markers for the influence of finite size effect, e. g. for a mean height above the stabilization of the homogeneous steady state results should be interpreted carefully with finite size effects in mind.

Figure 5.4 shows the height profiles corresponding to the labeled points in Figure 5.3. In Figure 5.4a the height profile number 4 shows how the height profile becomes almost sinusoidal before the branch merges again with the homogeneous branch at $h_0 = 5.07$. This is the bifurcation point, where the homogeneous steady state gains back linear stability. For the more wettable situation the single droplet branch merges with the homogeneous branch at $h_0 = 6.88$. The height profile number 3 in Figure 5.4a corresponds to the same mean height

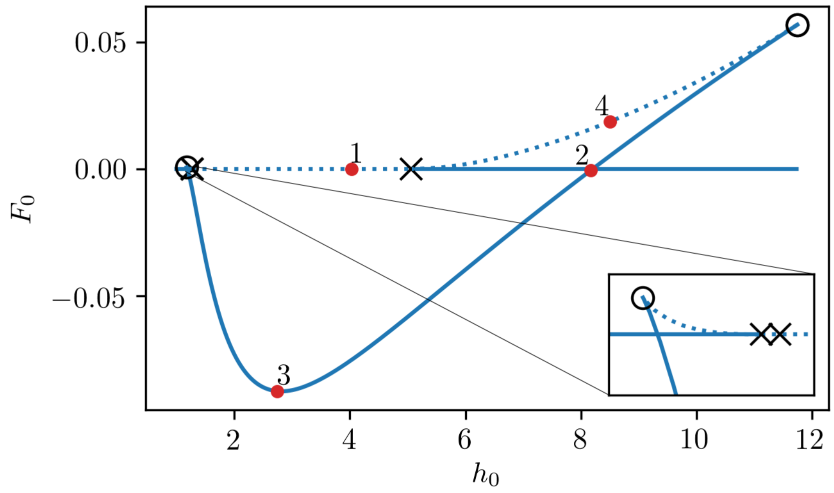

(a) High wettability with $\rho = \rho_{\text{HW}} = -0.12$

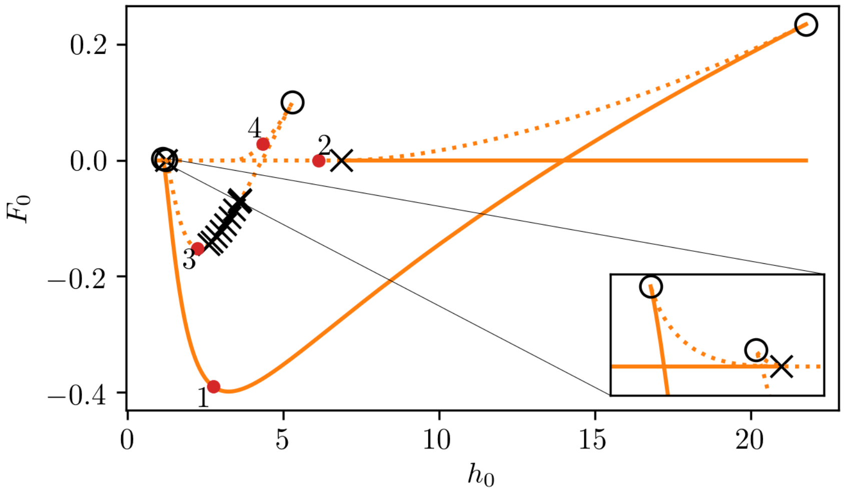

(b) Low wettability with $\rho = \rho_{\text{LW}} = 1.96$

Figure 5.3: Continuation in h_0 for ρ_{HW} (top) and ρ_{LW} (bottom) on a domain with size $L = 100$ and periodic boundary conditions. Fold points are marked with a circle and bifurcation points are marked with crosses. Insets show a zoom of the first bifurcation point. Dotted lines indicate linear instability and solid lines linear stability. The height profiles corresponding to the labeled points are shown in Figure 5.4.

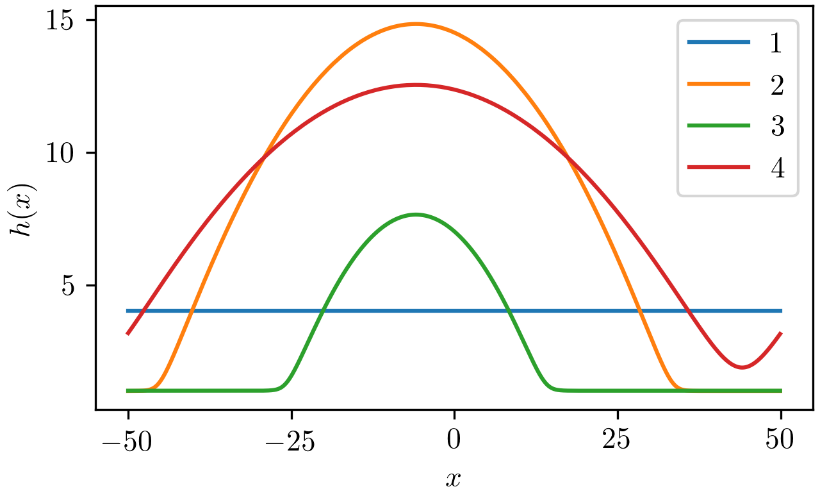

(a) High wettability with $\rho = \rho_{\text{HW}} = -0.12$

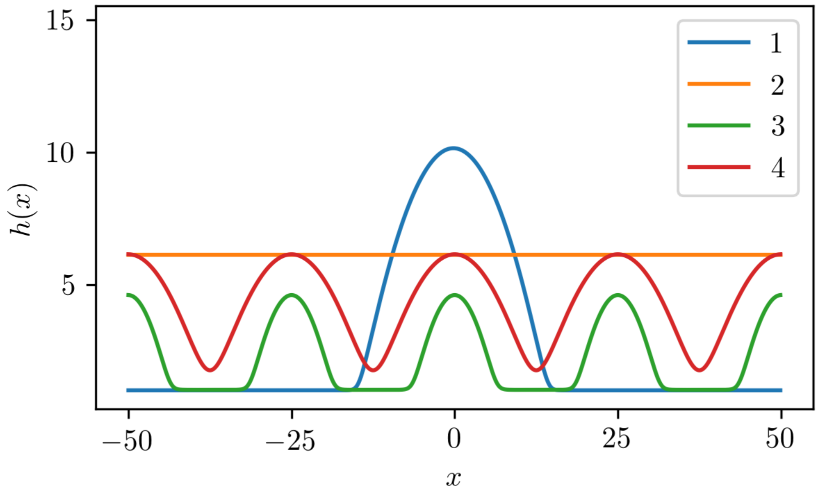

(b) Low wettability with $\rho = \rho_{\text{LW}} = 1.96$

Figure 5.4: Height profiles corresponding to the labeled points in Figure 5.3 for ρ_{HW} (top) and ρ_{LW} (bottom) on a domain with size $L = 100$ and periodic boundary conditions.

$h_0 = 2.75$ as height profile number 1 in Figure 5.4b. The different contact angles can be observed with the naked eye. Note that the scaling of the axes in the graph can distort the quantitative conception of the contact angles.

The height profile number 3 in Figure 5.4b depicts a four droplet shape. The height profile number 4 lies on the same branch, but it is shaped more sinusoidal. This is because the four droplet branch bifurcates from and merges back to the homogeneous branch qualitatively similar to the single droplet branch (cf. Figure 5.3b).

It is important to know the parameter space where single or multi droplet steady states can be found. In appendix A a simple estimation is derived, whether a droplet fits in a given domain depending on the contact angle Θ, the domain size L and the mean height h_0. It can be used to estimate the droplet size, if the net droplet volume is plugged in directly instead of calculating it via $V = (h_0 - h_p)L$ with the precursor film height h_p. In Figure 5.4a the height profile number 3 corresponds to a mean height of $h_0 = 2.75$ and a contact angle of $40°$, which yields an estimated droplet width w of $w = 37$. The estimation for height profile number 1 in the bottom part gives a droplet width of $w = 25$. Both estimations are considerably lower than the domain size. Thus finite size effects are not likely to make a significant difference in this case. If the droplet width is defined as the width w between the points, where the height is a tenth of the maximum net height $h_{\text{net}} = \max h - h_p$, the droplets with higher and lower wettability have a width of $w_{\text{HW}} = 38$ and $w_{\text{LW}} = 27$ respectively. This is reasonably close to the estimation.

5.3 INSTANT SWITCHING OF WETTABILITY

So far, possible steady states on a homogeneous surface have been investigated, but the continuation results with the help of the free energy measure used in Figure 5.3 can give additional insights into the system's behavior after an instant switch. The free energy is a Ljapunov functional for the system, which means that the free energy decreases monotonically in time. An instant change in wettability is directly connected to an instant change in free energy. Figure 5.5 visualizes how the continuation plots from Figure 5.3 look when the free energy with respect to the new wettability after an instant switch is applied as a measure. Assume a homogeneous film $h(x) = h_0$ with mean height $h_0 = 6.59$ and a high wettability $\rho_{\text{HW}} = -0.12$. Now the wettability changes instantly to the lower wettability ρ_{LW}. This situation corresponds to the red point in 5.5a. For the new wettability the homogeneous film is linearly unstable and thus an infinitesimal perturbation lets the height profile develop away from the homogeneous film. In Figure 5.5a the next steady state with a free energy below the red point corresponds to the single droplet steady state. Note that only the four droplet branch is shown and other multi droplet states could lie between the homogeneous and the single droplet branch. Nevertheless, the long-term height profile is likely to be droplet shaped, because the single droplet branch has the lowest free energy for this mean film height h_0.

In Figure 5.5b the red dot corresponds to the same mean height and a switch from the lower wettability ρ_{LW} to the higher wettability ρ_{HW}. At the new wettability there are three possible steady states with a lower free energy. One linearly unstable steady state belongs to a branch, which develops to the single droplet branch after a fold. The other two steady states are the linearly stable homogeneous film and the linearly stable single droplet steady state, which has the lowest free energy and thus is the expected long term result for the height profile. One possible transition to the single droplet state of the new wettability is via the homogeneous steady state.

5.4 TIME SIMULATIONS FOR SWITCHABLE WETTABILITIES

The continuations for a constant wettability have shown that the linearly stable state with the lowest free energy is the single droplet state for h_0 low enough except for values close to $h_0 = 1$. Direct numerical time simulations offer the possibility to investigate what happens if the wettability is switched periodically and instantaneously between the two wettabilities ρ_{LW} and ρ_{HW} after a certain switching period T. Before the periodic switching started a simulation was performed for a time $t_{\mathrm{relax}} = 200$ with the lower wettability ρ_{LW} to be sure that the starting point is exactly the single droplet steady state. The free energy plotted against the time is shown in Figure 5.6 for the switching periods $T_1 = 5$ and $T_2 = 200$. The longer switching period is enough for the droplet to settle on the substrate with the new wettability, so that in Figure 5.6b every switch in the same direction looks identical from the beginning.

In contrast, the shorter switching period shown in Figure 5.6a only repeats identically after a certain time. This is because the time to reach the lowest possible free energy for the respective wettability is greater than T_1.

Figure 5.6 gives an overview, but is not capable of showing differences between the switch directions. To investigate differences between switch directions Figure 5.7 shows a zoom on one particular switch for the longer switching period T_2. Both switching directions are plotted on top of each other with the maximum droplet height h_{max} and the contact angle Θ as a measure. The insets in Figure 5.7a and 5.7b zoom on the time directly after the switching process. The maximum droplet height depicts a small plateau, which spans over a longer time for the switch towards the lower wettability. The contact angle tends to the opposite of the expected direction directly after the switch. Again this

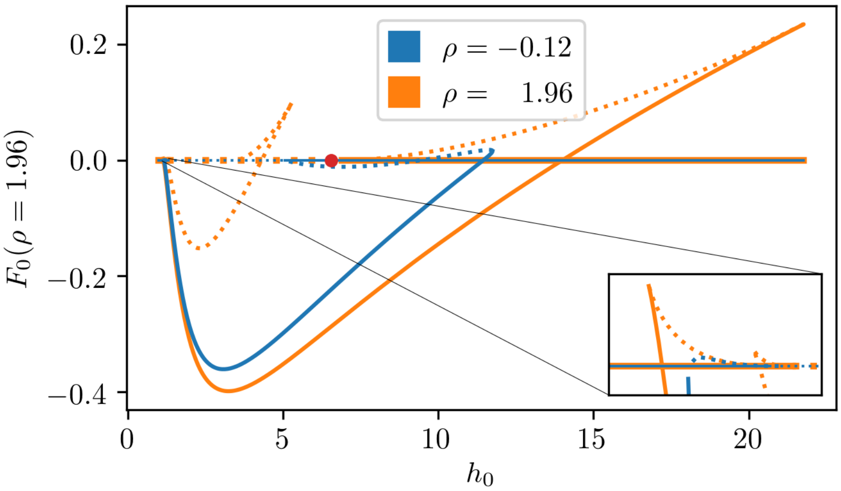

(a) Switch from lower to higher wettability ($\rho = -0.12 \rightarrow \rho = 1.96$)

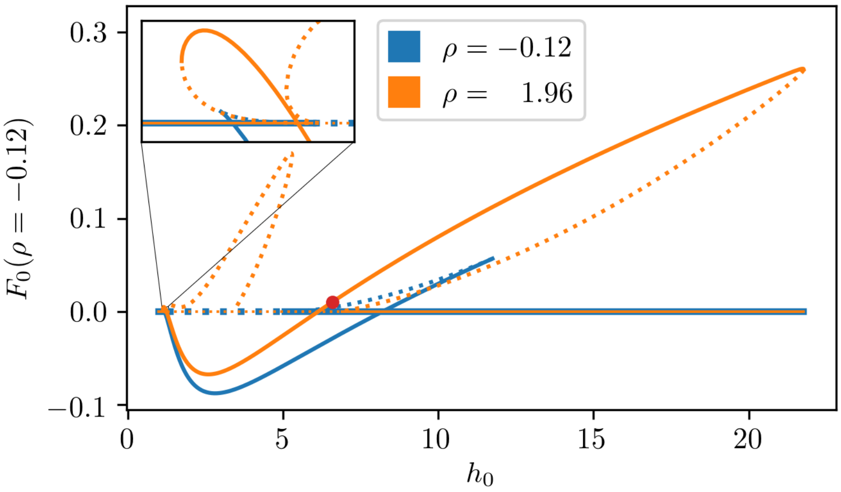

(b) Switch from higher to lower wettability ($\rho = 1.96 \rightarrow \rho = -0.12$)

Figure 5.5: Continuation plot with the free energy after an instant switch as a measure. Additionally, the steady states at the new wettability are shown. The red markers help to explain how these plots can be interpreted.

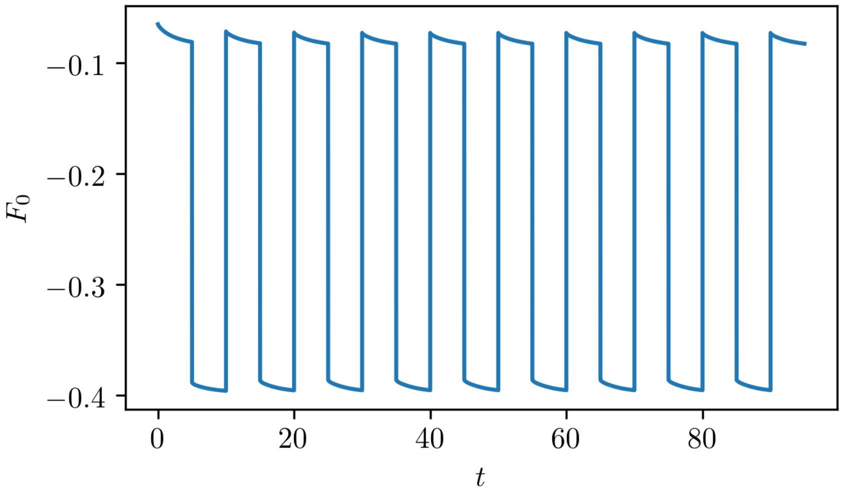

(a) Switching period $T = 200$

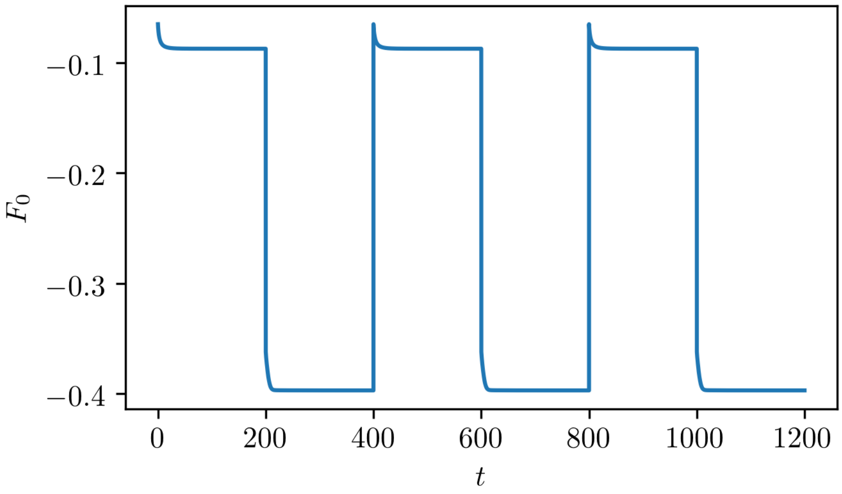

(b) Switching period $T = 5$

Figure 5.6: Development of the free energy $F_0(t)$ for periodic, instant switching between ρ_{HW} and ρ_{LW}. Switching periods are given in the subcaptions.

Table 5.1: Relaxation times for the different measures and different switching directions. Relexation times are calculated with equation 3.20 with the switching time $T_2 = 200$ as the threshold time t_{tr}.

ρ	$\tau[F_0]$	$\tau[h_{\max}]$	$\tau[\Theta]$
$\rho_{\mathrm{HW}} \to \rho_{\mathrm{LW}}$	4.8	13.7	12.5
$\rho_{\mathrm{LW}} \to \rho_{\mathrm{HW}}$	4.2	8.3	8.9

is emphasized for the switch towards the lower wettability. As a direct consequence the intersection of the curves is a few degrees below the middle of the initial values.

For the switching period $T = 5$ a zoom on one particular switch is shown in Figure 5.8. Analogously with Figure 5.7b the contact angle in Figure 5.8b starts to increase or decrease for the switch towards a higher or a lower wettability respectively, before it develops the expected way. In Figure 5.8a a similar behavior is shown, whereas in Figure 5.7a it is more like a plateau. Both diagrams in Figure 5.8 show that the stable state is not reached, i. e. the contact angle fluctuates between 55° and 67° although the stationary states correspond to the contact angles 40° and 75°. Again the lines intersect below the mean of the initial values.

The relaxation times calculated with equation 3.20 for the different measures are shown in Table 5.1. As Figure5.8 indicated, relaxation times differ depending on the switch direction, but additionally the free energy relaxes considerably faster than the maximum height and the contact angle. This means that the free energy measure is not a good choice to determine whether a stable state has already been reached or not, because a small change in the free energy can mean a notable change in the height profile. The relaxation times of the maximum height and the contact angle are roughly the same. All the relaxation times for $T = 200$ show that the stable state is reached faster, when starting from the lower wettability.

A direct comparison of the height profiles at the peak of the contact angle and the height profile immediately after the switch is shown in Figure 5.9. For the switch towards the lower wettability the height profiles are compared in Figure 5.9a. The differences of the height profile are hard to see if they are plotted in one graph. Therefore, the difference $\Delta h = h(t_2) - h(t_1)$ is plotted in the bottom row additionally. At the edge of the droplet there is a negative peak in the difference Δh, which means that the droplet gets narrower. The positive peak closer to the droplets center means that the flanks increase in height. Consequently, the droplet gets wider closer to the top. At $x = 0$ the difference is close to zero, which is in line with the results from Figures 5.7 and 5.8.

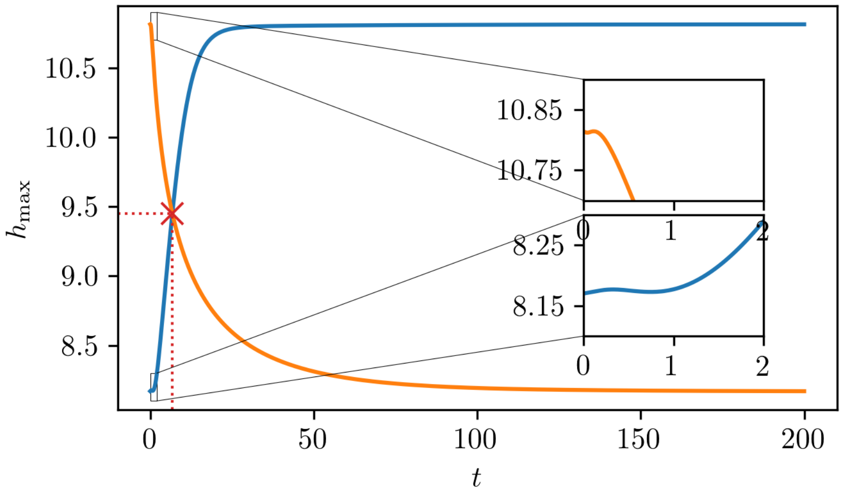

(a) Development of the maximum height h_{hmax}

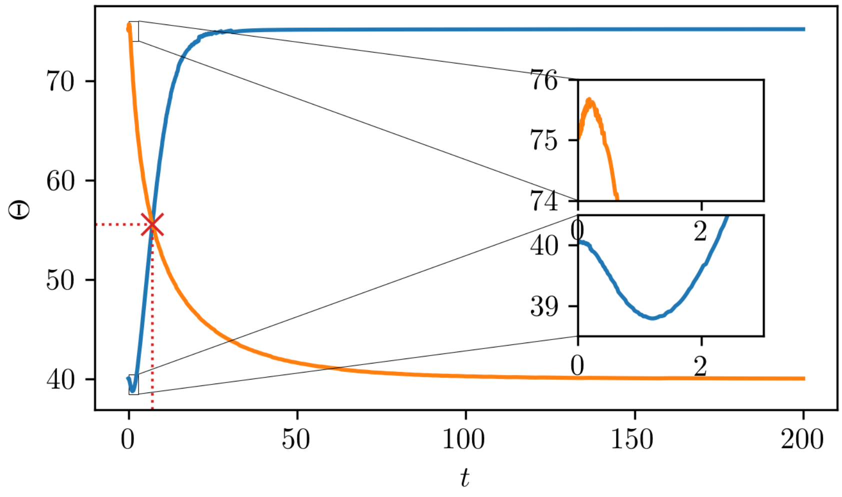

(b) Development of the contact angle Θ

Figure 5.7: Comparison of the switch direction and the adaption of the maximumg drop height $h_{\max}$ and the contact angle Θ for a switching period $T = 200$. The intersection is marked with a red cross. Insets zoom in on the time directly after the switch.

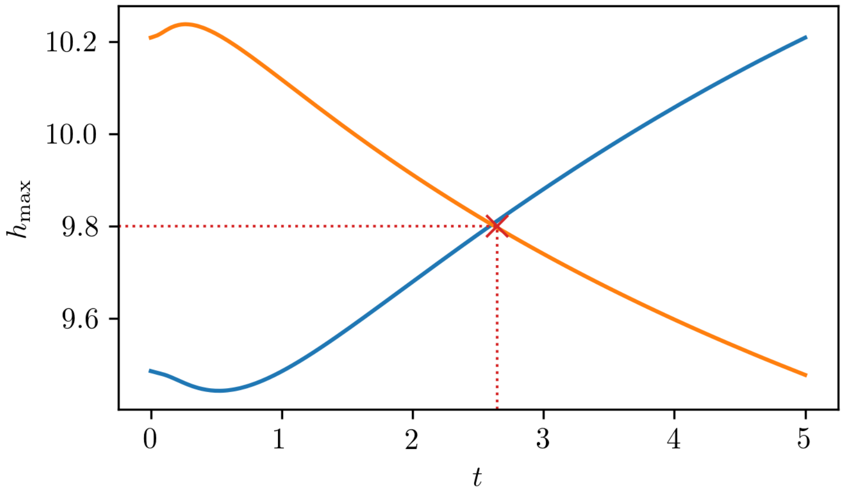

(a) Development of the maximum height $h_{\max}$

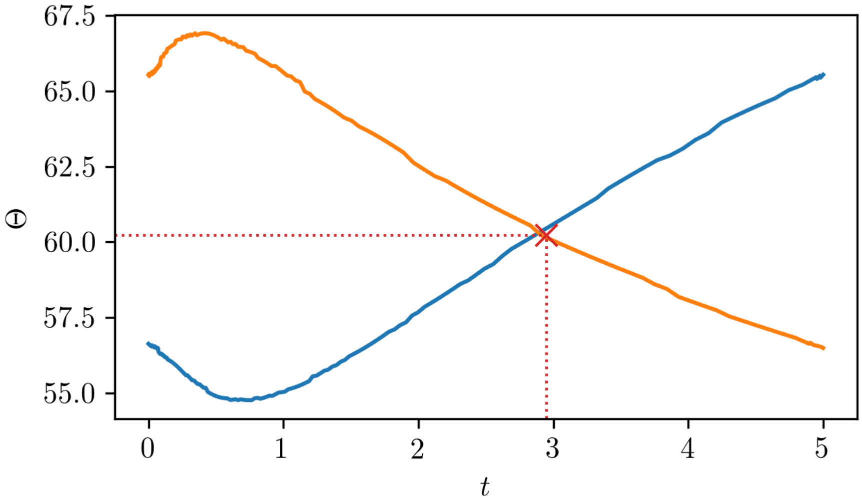

(b) Development of the contact angle Θ

Figure 5.8: Comparison of the switch direction and the adaption of the different measures for a switching period $T = 5$. The intersection is marked with a red cross.

These observations explain the evolution of the contact angle directly after a switch. Only points with more than 2/3 of the maximum height influence the computed contact angle. So it is not important that the base of the droplet gets narrower. The wider top and a constant maximum height lead to the observed, small decrease of the contact angle. Similar reasoning can be applied to Figure 5.9b only that the top decreases in width, which leads to an increased contact angle. This phenomenon is not entirely based on the way the contact angle is computed, as the wider or narrower top is considered in the contact angle computation. However, the actual origin of this phenomenon is not known.

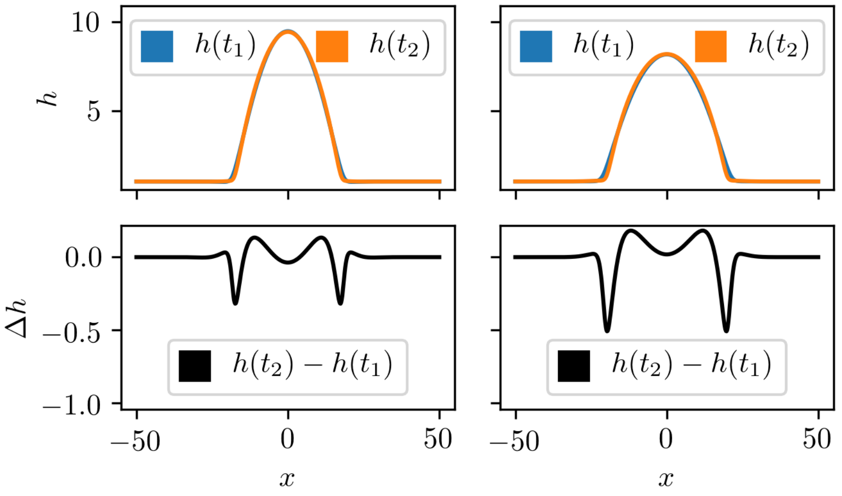

(a) Height profile difference immediately after switch from ρ_{HW} to ρ_{LW} for $T = 5$(left) and $T = 200$(right).

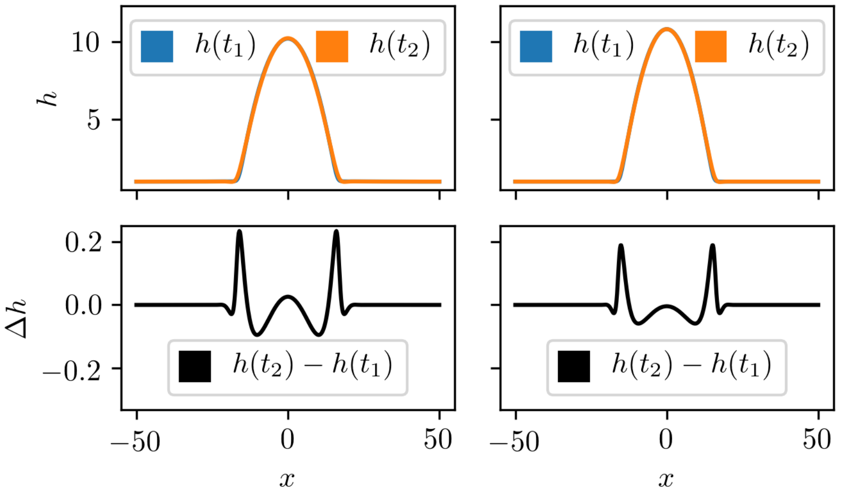

(b) Height profile difference immediately after a switch from ρ_{LW} to ρ_{HW} for $T = 5$(left) and $T = 200$(right).

Figure 5.9: Immediate change of the height profile after an instantaneous change in wettability. The top rows show the height profiles at the next timestep after the switch t_1 and at the point t_2 with the highest and lowest contact angle for a switching direction from high to low and low to high wettability respectively. The bottom rows show the difference between the height profiles in the top rows.

6

LIQUID ON PRESTRUCTURED SUBSTRATE

A prestructured substrate consists of at least two regions with different wettabilities connected by a transition zone. One possibility to introduce a stripe prestructure is

$$\rho g(x) = \rho_0 + \Delta\rho \cdot \tanh \frac{x + x_A}{l_s} \cdot \tanh \frac{x - x_A}{l_s}. \qquad (6.1)$$

Here the abbreviations $\Delta\rho = (\rho_{\mathrm{LW}} - \rho_{\mathrm{HW}})/2$ and $\rho_0 = (\rho_{\mathrm{LW}} + \rho_{\mathrm{HW}})/2$ are introduced. The geometric properties can be tuned via the parameters x_A corresponding to half the width of the patch with higher wettability centered at $x = 0$ and l_s corresponding to the steepness of the transition between the two wettabilities. Figure 6.1 shows a plot of equation 6.1 visualizing the parameters' influence on the shape of the prestructure. The prestructure shown in Figure 6.1 is denoted "Center HW" in the following, because the center region has a wettability of ρ_{HW} and the outside region has a wettability of ρ_{LW}. A sign change of $\Delta\rho$ yields the prestructure denoted "Center LW" in the following. For this configuration the wettabilities of the center and the outside region are exchanged compared to "Center HW".

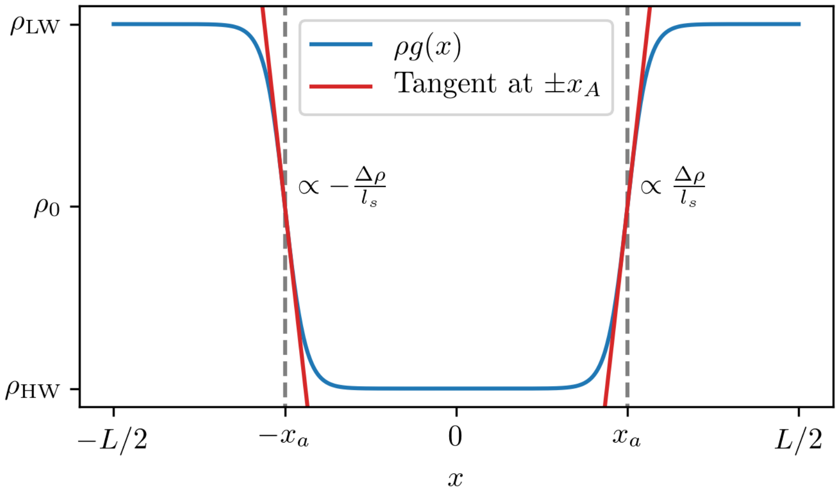

Figure 6.1: Inhomogeneous prestructure according to equation 6.1. The middle of the transition region at $x = \pm x_a$ is marked with a dashed grey line. The slope at $x = \pm x_a$ is directly connected to the parameters $\Delta\rho$ and l_s.

6.1 CONTINUATION FOR CONSTANT WETTABILITY

A continuation in the mean film height h_0 is shown in Figure 6.2. The qualitative shape of the single droplet branch starting at $h_0 = 0$ is comparable to the shape of the single droplet branch for a homogeneous substrate except for values of h_0 close to one (cf. Figure 5.3). Due to the prestructure the homogeneous film $h(x) = h_0$ is not a steady state. Consequently, the single droplet steady state cannot bifurcate from the homogeneous steady state, instead it is the only steady state found for h_0 close to one.

For the high wettable center an additional, partly linearly stable branch is shown in Figure 6.2a. This branch was not fully continued, because the discovered steady states had multiple unstable eigenvalues and thus are not as relevant for the dynamics as linearly stable steady states. Additionally, a required step size of $\mathrm{d}s = 1 \times 10^{-8}$ in parts of the branches makes the computation time intensive. So far no bifurcation point connecting both branches could be detected. The height profiles corresponding to the light blue branch are shown in the appendix B.

For the prestructure with a lower center wettability the inset in Figure 6.2b shows two folds occurring at mean film heights $h_0 = 1.15$ and $h_0 = 1.19$. The qualitatively different height profiles before the first fold, between these two folds and after the second fold are shown in the appendix B.

The linearly stable height profiles are shown in Figure 6.3. For a mean film height of $h_0 = 5$ there are three possible droplet steady states, which are shown in the continuation diagrams. For the more wettable center both droplet steady states have a similar contact angle of approximately 75°, because the edges of the droplet centered at $x = 0$ are already on the less wettable parts of the substrate. The height profiles corresponding to free energies close to zero are shown in Figure 6.3b. Due to the stripe prestructure the film height on the more wettable part of the prestructure is higher than on the less wettable part. For higher mean film heights h_0 the difference between the maximum and the minimum film height decreases, as the influence of the prestructure decreases.

6.2 INSTANT SWITCHING OF WETTABILITY

The Figure 6.4 visualizes the possible height profiles after an instant switch. A switch from a higher center wettability towards a lower center wettability guarantees a droplet steady state for mean film heights below $h_0 = 7.50$ as the final state. The initial height profile before a switch does not influence the final steady state, if the initial state is a steady state, as both the light blue and the dark blue branch have a higher free energy than the final droplet steady state. Nevertheless,

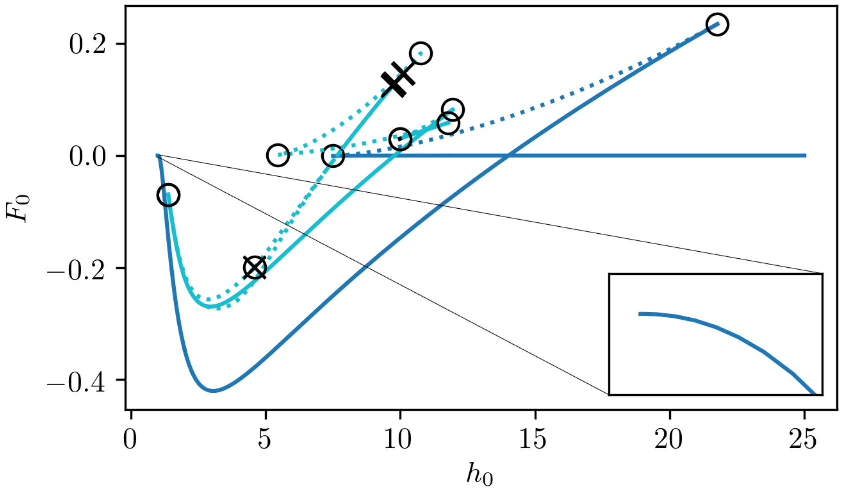

(a) Center with high wettability ρ_{HW} (Center HW). The light blue and the dark blue branch are not connected. Different colors are chosen to be able to differentiate the branches.

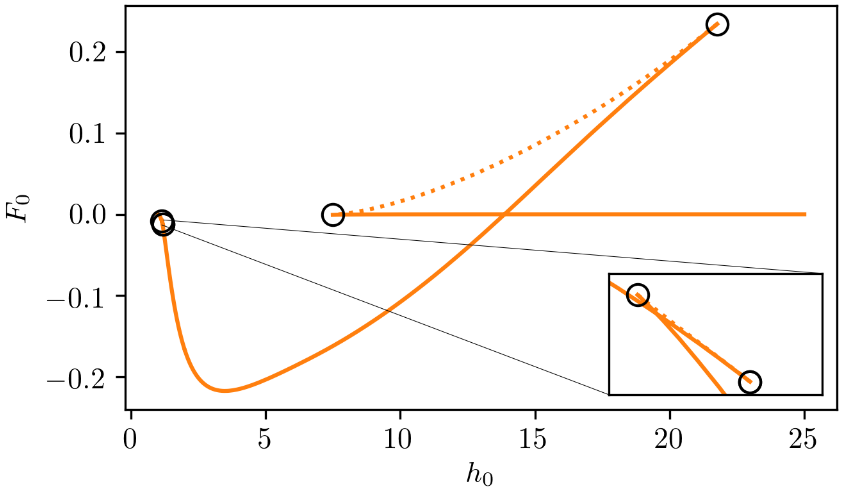

(b) Center with low wettability ρ_{LW} (Center LW).

Figure 6.2: Continuation in h_0 for a stripe prestructure. a) Center has a higher wettability than the outside. b) Center has a lower wettability than the outside. Fold points are marked with a circle and bifurcation points are marked with crosses. Dotted lines indicate linear instability and solid lines linear stability. Parameters are $L = 100$, $x_A = 12.5$ and $l_s = 1.5$.

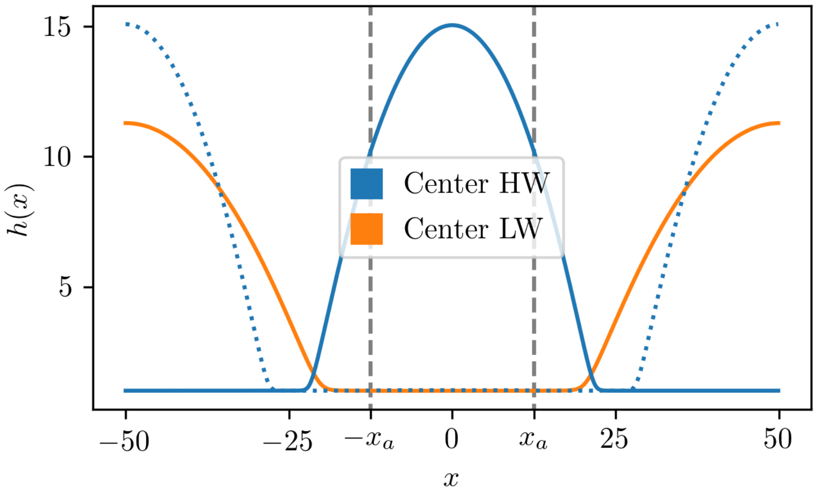

(a) Droplet steady states for a high and a low wettable center with a mean height $h_0 = 5$.

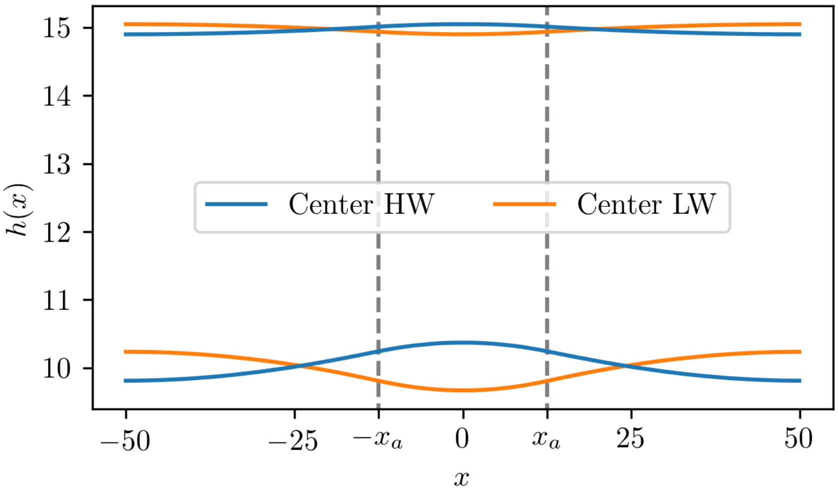

(b) Steady states with a free energy close to zero for the mean heights $h_0 = 10$ and $h_0 = 15$.

Figure 6.3: Comparison of height profiles of the prestructure with a higher wettability in the center (Center HW) and a low wettability in the center (Center LW).

the relaxation time and the path towards the new steady state is still influenced by the initial height profile, i. e. the diagrams shown in Figure 6.4 can only help to find the possible final steady state, but they cannot determine the temporal behavior.

The droplet steady state corresponding to the solid part of the light blue branch is centered at $x = \pm 50$, the same spot the droplet corresponding to the orange branch is centered at. This suggests that the relaxation time for such a switch is lower than starting from a droplet located at the center, because the center droplet has to move or diffuse via the precursor film to reach the location of the new steady state.

For the reverse switching direction (Center LW → Center HW) for mean film heights below $h_0 = 7.50$ two different linearly stable droplet steady states are possible (cf. Figure 6.4b). Additionally, some linearly unstable steady states can be reached. However, numerical continuation does not allow to make conclusions about which state will be reached and how it is reached.

6.3 TIME SIMULATIONS FOR SWITCHABLE WETTABILITIES

Figure 6.5 shows height profiles from a time simulation for two sequential switches from Center HW to Center LW and back. The switching period is $T = \infty$, which means that the switch in the reverse direction is performed when a steady state is reached. Figure 6.6 shows the corresponding evolutions of the free energy and the contact angle. The initial height profile with the index one is the droplet steady state centered at $x = 0$. After the switch the droplet shape adapts to the new prestructure. This means the free energy decreases and the contact angle increases to around 70°. Then the droplet starts to move away from the less wettable center. As soon as the droplet moves through the transition zone the free energy decreases again. The contact angle does not decrease monotonically until the contact angle of the steady state is reached. Instead it increases again, when the peak is in the transition zone. After a time $\Delta t \approx 1000$ a stationary state for the new wettability is reached. The new stationary state is centered at $x = 39.1$. The reverse switch does not inverse the height profile as well. The droplet only adapts its shape to the new wettability and does not move. The contact angle of the final steady state is $\Theta = 73.2°$. The final state with index seven has a higher free energy for the stripe prestructure with a higher center wettability than the initial state with index one. This means the free energy is at a local minimum and not at the global minimum. The final state lies on the light blue branch of the continuation diagram shown in Figure 6.2a.

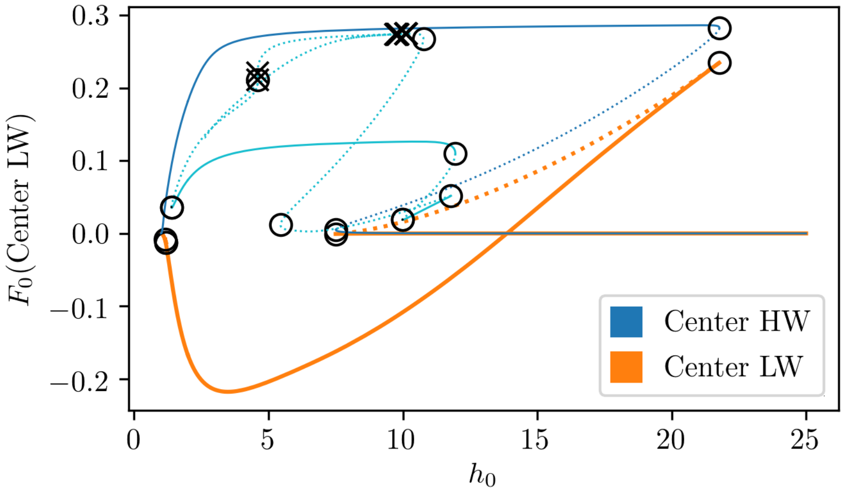

(a) Switch from a center with higher wettability ρ_{HW} to a center with lower wettability ρ_{LW}.

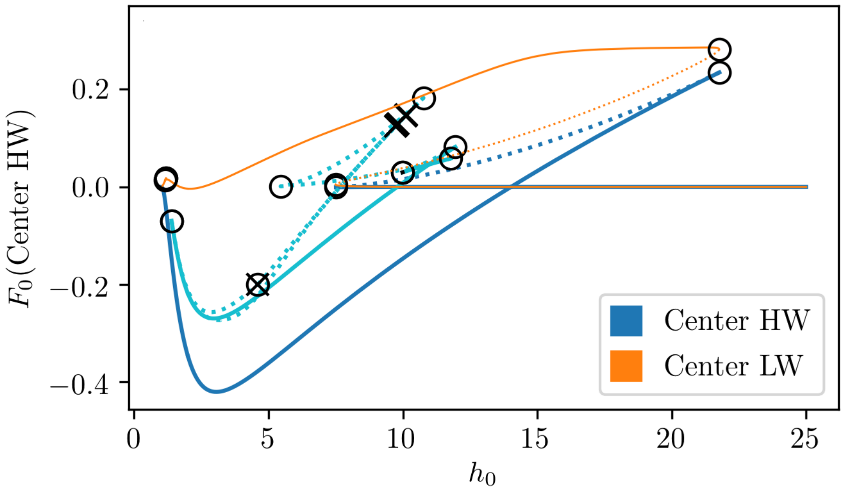

(b) Switch from a center with lower wettability ρ_{LW} to a center with higher wettability ρ_{HW}.

Figure 6.4: Continuation plot with the free energy after an instant switch as a measure. Additionally, the steady states at the new wettability are shown. For the stripe prestructure with a high center wettability two branches are shown, which are not connected via a bifurcation. To be able to differentiate them one branch is shown in a lighter blue.

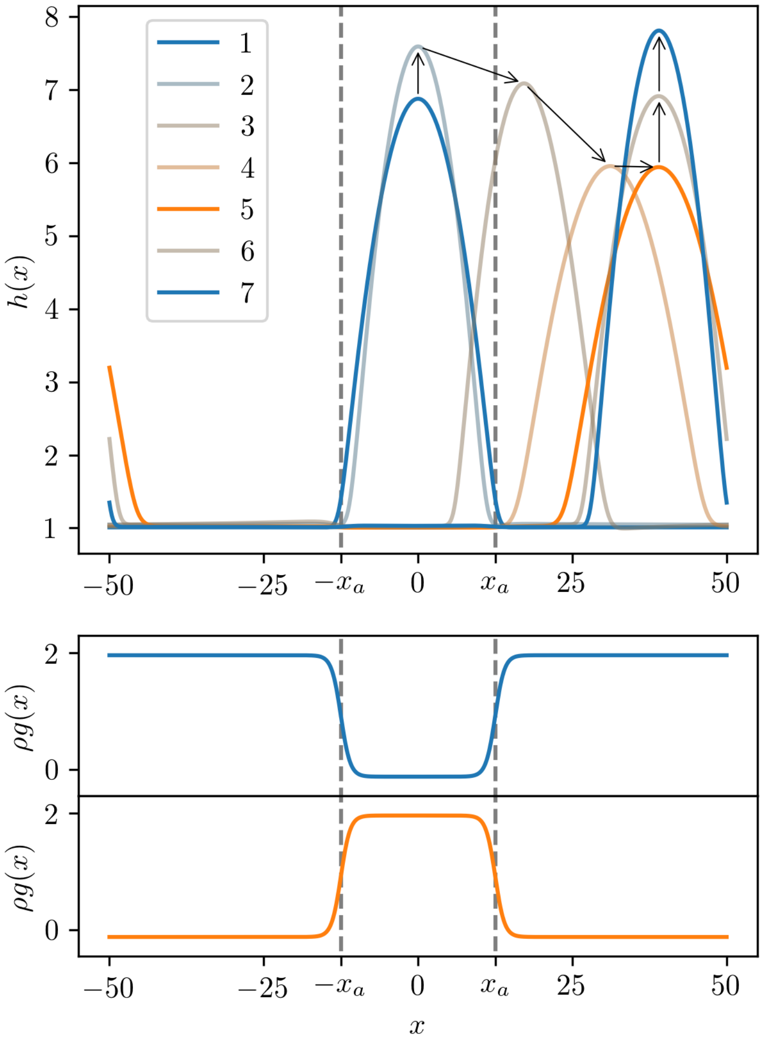

Figure 6.5: Height profiles from a time simulation (top) for two sequential switches (Center HW → Center LW → Center HW). The blue height profiles correspond to the stationary solutions for Center HW. The orange height profile correspond to the stationary solution for Center LW. The semi transparent height profiles are intermediate height profiles to visualize the transition. The corresponding wettabilities are shown in the bottom. The numbers in the legend match the numbered red points in Figure 6.6. The mean film height in the time simulation is $h_0 = 2$.

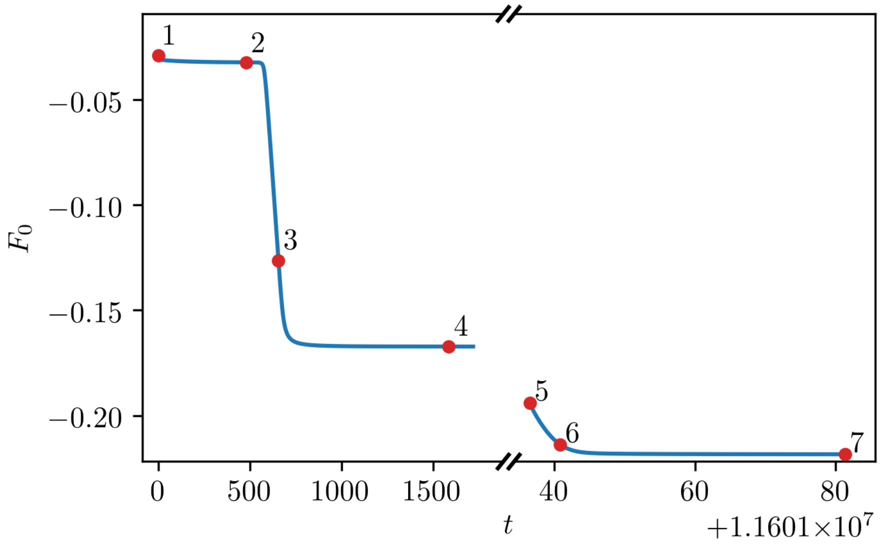

(a) Temporal evolution of the free energy F_0.

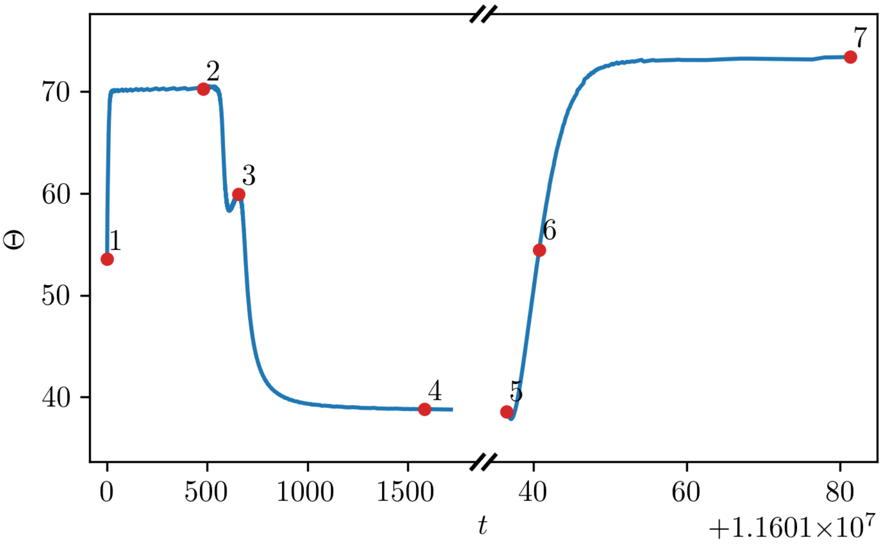

(b) Temporal evolution of the contact angle Θ.

Figure 6.6: Evolution of the free energy F_0 (top) and the contact angle Θ (bottom) for two sequential switches (Center HW → Center LW → Center HW). The free energy is calculated with respect to the wettability at the current time. The initial height profile at $t = 0$ is the droplet steady state centered at $x = 0$ (Center HW). The second switch is performed after a stationary state has been reached, i. e. the time step dt gets bigger than 1×10^6. The mean film height in this time simulation is $h_0 = 2$.

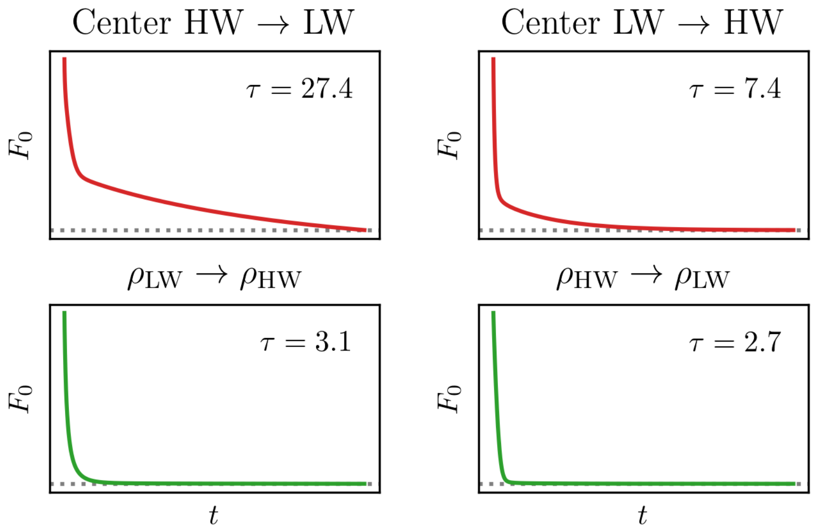

Figure 6.7: Comparison of relaxation times for both switching directions on a homogeneous substrate and on a prestructured substrate for the switching period $T = 200$ on a domain size $L = 100$ with a mean film height $h_0 = 2$. The dotted grey lined indicate the final value reached.

The same switching process (Center HW → Center LW → Center HW) for a lower switching period $T = 200$ exhibits a different behavior, as the droplet has not enough time to move away from the center. Thus only the contact angle adapts from $\Theta = 53.6°$ to $\Theta = 70.2°$. Directly after the switch the contact angle exhibits a similar behavior compared to the homogeneous substrate, i. e. initially it develops contrary to the expected direction. However, the prestructure makes a difference as far as relaxation times are concerned. Figure 6.7 compares the evolution of the free energy for the homogeneous substrate and the stripe prestructure. The relaxation times on substrate with a stripe prestructure are significantly higher than on a homogeneous substrate even though the free energy does not show a plateau, which would indicate that a meta state is involved. The contact angle on the homogeneous substrate adapts from 38.6° to 73.4° and back. This implies that the general shape changes more on a homogeneous substrate and the relaxation time should be higher. As this is not the case, the different relaxation times can probably be solely attributed to the prestructure.

7

CONCLUSION AND OUTLOOK

In this thesis the necessary driver's code to do continuations in PDE2PATH and direct numerical simulations in OOMPH-LIB has been developed for 1D and 2D domains. Additionally, an interface to access the Matlab specific `.mat` files from within OOMPH-LIB has been developed making use of the Matlab Data API and the Matlab Engine API. The interface can be improved with additional generalization to ease the adaption to a particular set of PDEs.

On this basis an analysis of a liquid on a homogeneous substrate and on a prestructured substrate has been performed in 1D. The Lyapunov functional property of the free energy has been exploited to extract informations on possible behavior after a change in wettability. Switching periods in the order of magnitude of the relaxation time prevent the system from reaching the steady states. A prestructure can influence the relaxation time. Figure 6.7 shows that in this case the relaxation time is significantly increased.

Immediately after switching the wettability the contact angle shows an unexpected behavior, as it develops into the opposite of the expected direction for a short amount of time (cf. Figure 5.7). A closer analysis of the height profiles shown in Figure 5.9 can explain, why such contact angles are computed for the involved height profiles. The origin of this effect is not clear, although it is unlikely solely an artifact of the contact angle calculation.

Changing the wettability for enough time to reach the steady state and then switching back can make it possible to reach states, which are not global but only local minima of the free energy. This is shown in Figure 6.5.

So far it was only shown that a switchable wettability provides a mean to manipulate the pattern formation. To expand the work presented here switching strategies could be developed to be able to manipulate the pattern formation in a controlled manner. An extension to the 2D case would improve the model, because some instabilities do not occur in the 1D case. The investigation of the 2D case is possible on the basis of the code developed during this master thesis, as it already accounts for the 2D case. Additionally, more stripes can be added to the prestructure to be able to investigate ridge interaction.

APPENDIX

A

ESTIMATION OF THE MINIMUM REQUIRED DOMAIN SIZE

Suppose one wants to know if a droplet with a contact angle Θ fits on a domain with size L at a given mean height h_0. One way to estimate the lateral expansion of the droplet is to estimate its volume from the assumption that it is shaped like a perfect spherical cap (cf. contact angle measurement in section 3). Such a height profile can be formulated as

$$h(x) = \sqrt{R^2 - x^2} - y_c, \tag{A.1}$$

with the y-Position of the center y_c and the radius R. The droplet is assumed to be centered at $x = 0$. The net droplet volume is given as

$$V = \left(h_0 - h_p\right) \cdot L. \tag{A.2}$$

from the mean height h_0 and the domain size L. Similar to (3.15) the contact angle is related to the height profile via

$$\tan\Theta = \left| \left.\frac{\partial h}{\partial x}\right|_{h=h_p} \right|. \tag{A.3}$$

Another way to determine the net droplet volume is via an integration of the height profile. As boundary values the x-position with $h = h_p$ is needed. Equation (A.1) yields

$$\tilde{x} = \sqrt{R^2 - \left(h_p + y_c\right)}. \tag{A.4}$$

With the help of some algebra equation (A.3) yields the relations

$$\begin{aligned} \tan\Theta &= \sqrt{\frac{R^2}{\left(h_p + y_c\right)^2} - 1}, && \text{(A.5)} \\ R^2 &= \left(h_p + y_c\right)^2 \left(\tan^2\Theta + 1\right) && \text{(A.6)} \\ \text{and} \quad \left(h_p + y_c\right)^2 &= \frac{R^2}{\left(\tan^2\Theta + 1\right)}. && \text{(A.7)} \end{aligned}$$

Executing the integral gives

$$\begin{aligned} V &= \int_{\tilde{x}}^{\tilde{x}} \big(h(x) - h_p\big) dx \\ &= \frac{1}{2} x \sqrt{R^2 - x^2} + \frac{1}{2} R^2 \arctan\left[\frac{x}{\sqrt{R^2 - x^2}}\right] - (h_p + y_c) x \Big|_{\tilde{x}}^{\tilde{x}} \\ &= \tilde{x} \sqrt{R^2 - \tilde{x}^2} + R^2 \arctan\left[\frac{\tilde{x}}{\sqrt{R^2 - \tilde{x}^2}}\right] - 2\big(y_c{+}_p\big)\tilde{x} \\ &\overset{(A.3)}{=} R^2 \Theta - \big(y_c + h_p\big)\tilde{x} \\ &\overset{(A.4)}{=} R^2 \Theta - \big(y_c + h_p\big) \sqrt{R^2 - (y_c + h_p)} \end{aligned}$$

Combined with equation (A.7) the expression

$$R^2 = \frac{V}{\Theta - \frac{\tan\Theta}{\tan^2\Theta + 1}} \tag{A.8}$$

for R^2 is obtained. Inserted into equation (A.4) with the help of equation (A.7)

$$\begin{aligned} \tilde{x} &= \sqrt{\frac{V}{\Theta - \frac{\tan\Theta}{\tan^2\Theta+1}} \cdot \left[1 - \frac{1}{\tan^2\Theta + 1}\right]} \qquad \text{(A.9)} \\ &= \sqrt{\frac{(h_0 - h_p) \cdot L}{\Theta - \frac{\tan\Theta}{\tan^2\Theta+1}} \cdot \left[1 - \frac{1}{\tan^2\Theta + 1}\right]} \qquad \text{(A.10)} \end{aligned}$$

results. With this result it is possible to calculate the droplet width $w = 2\tilde{x}$ and compare it to the domain size L. To avoid finite size effects the relation $w \ll L$ should hold.

B

ADDITIONAL HEIGHT PROFILES

This chapter shows additional height profiles not shown in the main part. Figure B.1 shows height profiles corresponding to points in the inset of Figure 6.2b. Figure B.2 shows height profiles and their location in the continuation diagram shown in Figure 6.2a before.

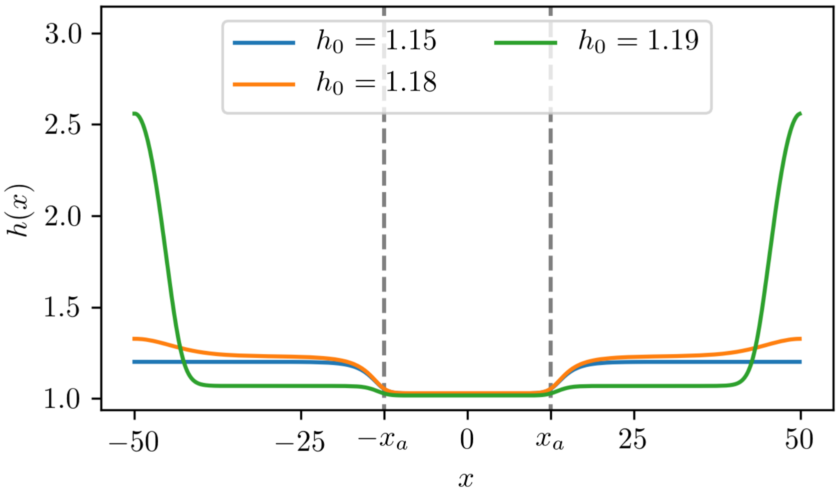

Figure B.1: Height profiles for a stripe prestructure and a low center wettability corresponding to the inset in Figure 6.2b. The orange height profile lies on the linearly unstable part of the branch shown in the insets. The mean film height h_0 is given in the legend.

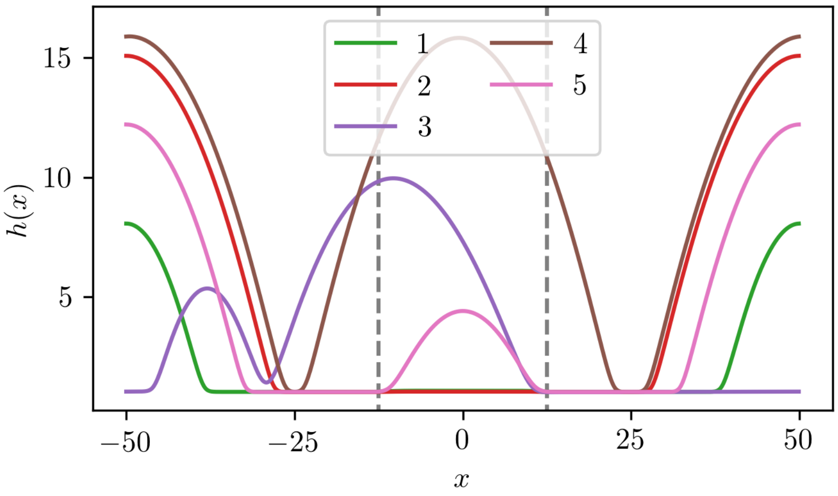

(a) Height profiles corresponding to the marked points shown in b.

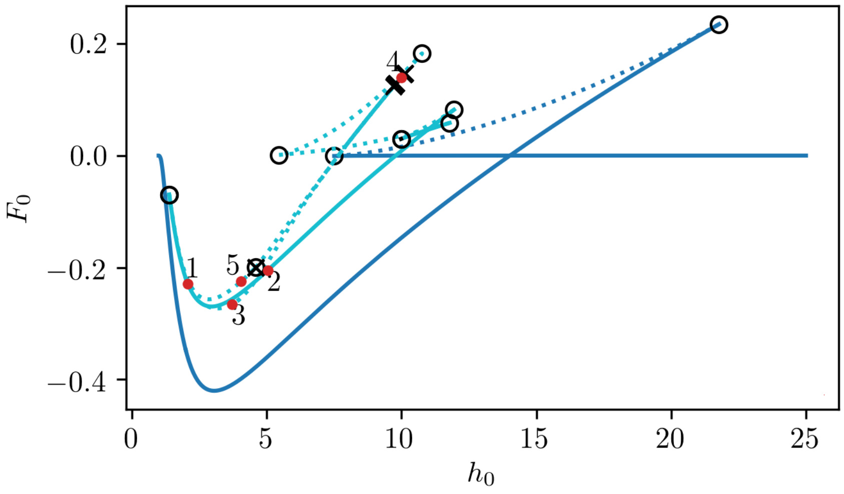

(b) Continuation diagram in h_0 with points corresponding to the height profiles shown in a.

Figure B.2: Height profiles for a stripe prestructure and a high center wettability (top) and corresponding bifurcation diagram (bottom). The numbers in the upper diagram correspond to the marked points in the bottom. The continuation diagram without the marked points is shown in Figure 6.2a as well.

BIBLIOGRAPHY

[1] S. Maenosono, T. Okubo, and Y. Yamaguchi. "Overview of Nanoparticle Array Formation by Wet Coating." In: *Journal of Nanoparticle Research* 5.1 (2003), pp. 5–15. DOI: `10.1023/A:1024418931756` (cit. on p. 1).

[2] U. Thiele. "Patterned deposition at moving contact lines." In: *Advances in Colloid and Interface Science* 206 (2014). Manuel G. Velarde, pp. 399–413. DOI: `https://doi.org/10.1016/j.cis.2013.11.002` (cit. on pp. 1, 3).

[3] A. Oron, S. H. Davis, and S. G. Bankoff. "Long-scale evolution of thin liquid films." In: *Rev. Mod. Phys.* 69 (3 1997), pp. 931–980. DOI: `10.1103/RevModPhys.69.931` (cit. on p. 1).

[4] L. W. Schwartz and R. V. Roy. "Theoretical and numerical results for spin coating of viscous liquids." In: *Physics of Fluids* 16.3 (2004), pp. 569–584. DOI: `10.1063/1.1637353` (cit. on pp. 1, 3).

[5] S. K. WILSON, R. HUNT, and B. R. DUFFY. "The rate of spreading in spin coating." In: *Journal of Fluid Mechanics* 413 (2000), pp. 65–88. DOI: `10.1017/S0022112000008089` (cit. on pp. 1, 3).

[6] W. Wang and L. Chi. "Area-Selective Growth of Functional Molecular Architectures." In: *Accounts of Chemical Research* 45.10 (2012). PMID: 22830409, pp. 1646–1656. DOI: `10.1021/ar200299w` (cit. on p. 1).

[7] W. Wang, C. Du, C. Wang, M. Hirtz, L. Li, J. Hao, Q. Wu, R. Lu, N. Lu, Y. Wang, H. Fuchs, and L. Chi. "High-Resolution Triple-Color Patterns Based on the Liquid Behavior of Organic Molecules." In: *Small* 7.10 (2011), pp. 1403–1406. DOI: `10.1002/smll.201002210` (cit. on p. 1).

[8] C. Honisch, T.-S. Lin, A. Heuer, U. Thiele, and S. V. Gurevich. "Instabilities of Layers of Deposited Molecules on Chemically Stripe Patterned Substrates: Ridges versus Drops." In: *WOS:000362243600036* (2015) (cit. on pp. 1, 3 sq.).

[9] W. Tewes, O. Buller, A. Heuer, U. Thiele, and S. V. Gurevich. "Comparing kinetic Monte Carlo and thin-film modeling of transversal instabilities of ridges on patterned substrates." In: *The Journal of Chemical Physics* 146.9 (2017), p. 094704. DOI: `10.1063/1.4977739` (cit. on pp. 1, 3 sq.).

[10] I. Berbezier, M. Aouassa, A. Ronda, L. Favre, M. Bollani, R. Sordan, A. Delobbe, and P. Sudraud. "Ordered arrays of Si and Ge nanocrystals via dewetting of pre-patterned thin films." In:

Journal of Applied Physics 113.6 (2013), p. 064908. DOI: `10.1063/1.4790713` (cit. on p. 1).

[11] N. Wagner and P. Theato. "Light-induced wettability changes on polymer surfaces." In: *Polymer* 55.16 (2014). Polymerized Ionic Liquids, pp. 3436–3453. DOI: `https://doi.org/10.1016/j.polymer.2014.05.033` (cit. on p. 1).

[12] U. Thiele and E. Knobloch. "On the depinning of a driven drop on a heterogeneous substrate." In: *New Journal of Physics* 8.12 (2006), pp. 313–313. DOI: `10.1088/1367-2630/8/12/313` (cit. on p. 3).

[13] U. Thiele. "Thin film evolution equations from (evaporating) dewetting liquid layers to epitaxial growth." In: *Journal of Physics: Condensed Matter* 22.8 (2010), p. 084019. DOI: `10.1088/0953-8984/22/8/084019` (cit. on pp. 3 sq.).

[14] S. Engelnkemper. "Nichtlineare Analyse physikochemisch getriebener Entnetzung - Statik und Dynamik." PhD thesis. Westfälische Wilhelms-Universität Münster, 2017 (cit. on pp. 3 sqq., 19).

[15] S. Engelnkemper, M. Wilczek, S. V. Gurevich, and U. Thiele. "Morphological transitions of sliding drops: Dynamics and bifurcations." In: *Phys. Rev. Fluids* 1 (7 2016), p. 073901. DOI: `10.1103/PhysRevFluids.1.073901` (cit. on p. 3).

[16] MATLAB. *version 9.4.0 (R2018a)*. Natick, Massachusetts: The MathWorks Inc., 2018 (cit. on p. 7).

[17] H. Uecker, D. Wetzel, and J. Rademacher. "pde2path - a Matlab package for continuation and bifurcation in 2D elliptic systems." In: *Numerical Mathematics: Theory, Methods and Applications* 7 (2014), pp. 56–106 (cit. on p. 7).

[18] T. Dohnal, J. Rademacher, H. Uecker, and D. Wetzel. "pde2path 2.0: multi-parameter continuation and periodic domains." In: *Proceedings of 8th European Nonlinear Dynamics Conference* (2014) (cit. on p. 7).

[19] M. Heil and A. L. Hazel. "oomph-lib – An Object-Oriented Multi-Physics Finite-Element Library." In: *Fluid-Structure Interaction*. Ed. by H.-J. Bungartz and M. Schäfer. Berlin, Heidelberg: Springer Berlin Heidelberg, 2006, pp. 19–49 (cit. on pp. 7, 13).

[20] D. Braess. *Finite Elemente - Theorie, schnelle Löser und Anwendungen in der Elastizitätstheorie*. Springer Berlin Heidelberg, 2007 (cit. on pp. 7 sq., 10).

[21] K. Levenberg. "A method for the solution of certain non-linear problems in least squares." In: *Quarterly of applied mathematics* 2.2 (1944), pp. 164–168 (cit. on p. 12).

[22] D. Marquardt. "An Algorithm for Least-Squares Estimation of Nonlinear Parameters." In: *Journal of the Society for Industrial*

and Applied Mathematics 11.2 (1963), pp. 431–441. DOI: `10.1137/0111030` (cit. on p. 12).

[23] R. Seydel. *Practical bifurcation and stability analysis*. Vol. 5. Springer Science & Business Media, 2009 (cit. on p. 14).

SELBSTSTÄNDIGKEITSERKLÄRUNG DES STUDIERENDEN

Hiermit versichere ich, dass die vorliegende Arbeit über

Dynamics of droplets on switchable prestructured substrates

selbstständig verfasst worden ist, dass keine anderen Quellen und Hilfsmittel als die angegebenen benutzt worden sind und dass die Stellen der Arbeit, die anderen Werken - auch elektronischen Medien - dem Wortlaut oder Sinn nach entnommen wurden, auf jeden Fall unter Angabe der Quelle als Entlehnung kenntlich gemacht worden sind.

(Ort, Datum, Unterschrift)

Ich erkläre mich mit einem Abgleich der Arbeit mit anderen Texten zwecks Auffindung von Übereinstimmungen sowie mit einer zu diesem Zweck vorzunehmenden Speicherung der Arbeit in eine Datenbank einverstanden.

(Ort, Datum, Unterschrift)